Angiogenesis (2026) 29:38
https://doi.org/10.1007/s10456-026-10059-3

ORIGINAL PAPER

Prevascularized grafts with spatially organized MSC spheroids to accelerate therapeutic angiogenesis in ischemic disease

Jeonghyun Son[1,2] · Aruzhan Naren[1,3] · Hanan Jamal Mohamed[1] · Minjun Ahn[4] · Won Ha[1,5] · Min Kyeong Kim[1] et al. ***[full author details at the end of the article]***

Received: 14 October 2025 / Accepted: 22 May 2026

Abstract

Objective Ischemic diseases, characterized by impaired blood flow and progressive tissue necrosis, remain a major challenge in regenerative medicine. Surgical revascularization remains the gold standard for restoring blood flow in major vessels, but still shows limited effects on microvascular regeneration. To address this unmet need, various strategies in therapeutic angiogenesis have been explored to induce microvascular formation, including delivery of bioactive molecules, stem cells, or pre-vascularized grafts. However, injection-based approaches often suffer from off-target effects, and conventional implantable grafts lack sufficient angiogenic secretory activity. To address these limitations, we aimed to develop a dual-function prevascularized graft that accelerates neovascularization and promotes vascular integration to restore tissue perfusion in ischemic conditions.

Methods and results The graft was engineered by combining a microvascular pattern (μVP) with spatially organized mesenchymal stem cell (MSC) spheroids, fabricated via high-precision coprinting of endothelial cells and MSCs. Optimization of spheroid density and spatial arrangement enhanced VEGF secretion and increased host capillary infiltration nearly twofold. In a murine critical limb ischemia model, implantation of these engineered grafts achieved a 60% limb salvage rate and reduced limb loss by ~15%, representing a 4.5-fold improvement over conventional grafts. Histological and morphometric analyses confirmed reduced muscle degeneration, enhanced neovascularization, and seamless anastomosis between engineered and host vessels.

Conclusions These findings demonstrate a dual-functional graft that couples paracrine stimulation with structural vascular support, providing a promising regenerative strategy to promote therapeutic angiogenesis and ischemia therapy, while indicating its potential for preclinical and future clinical applications in ischemic disease.

Graphical abstract

Schematic illustration of engineered grafts designed to enhance secretion and vascular integration, thereby promoting therapeutic angiogenesis and restoring blood perfusion in hindlimb ischemia

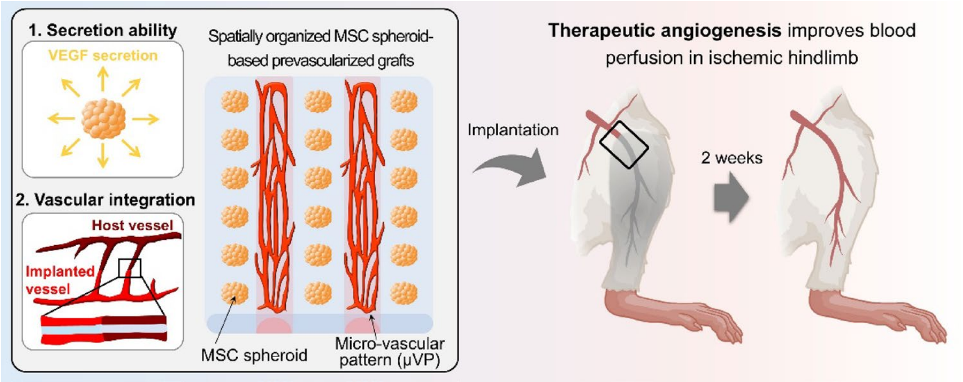

Keywords Regenerative medicine · Ischemia therapy · Therapeutic angiogenesis · Prevascularized grafts · Mesenchymal stem cell spheroids

Jeonghyun Son, Aruzhan Naren and Hanan Jamal Mohamed have contributed equally to this work.Abbreviations

ADSCs	Adipose derived stem cells
DAPI	4′,6-diamidino-2-phenylindole
ECs	Endothelial cells
GFP	Green fluorescent protein
H&E	Hematoxylin and eosin
LDPI	Laser doppler perfusion imaging
MT	Masson's trichrome
MSCs	Mesenchymal stem cells
PCL	Polycaprolactone
PSR	Picrosirius red
VEGF	Vascular endothelial growth factor
µVP	Microvascular pattern

Introduction

Ischemia is a pathological condition resulting from impaired blood circulation, resulting in insufficient delivery of oxygen and nutrients to tissues [1]. When prolonged, it can cause tissue necrosis, resulting in irreversible damage or life-threatening outcomes [2]. An example includes myocardial infarction caused by coronary artery occlusion, which remains one of the leading causes of mortality worldwide [3, 4]. In current clinical practice, surgical revascularization is widely employed [5, 6]. Procedures such as stenting or catheterization reopen occluded vessels and restore blood flow, offering the advantage of rapid functional recovery [7, 8]. However, these approaches primarily target large arteries and have limited applicability owing to interpatient anatomical variability and the risk of periprocedural complications [9]. Additionally, restenosis can occur post-procedure, while the surrounding microvasculature often fails to regenerate spontaneously, representing a major surgical revascularization limitation [10, 11]. Without re-establishing the dense capillary networks responsible for local oxygen and nutrient delivery, the functional recovery of affected tissues remains restricted [12, 13].

To address these clinical limitations, therapeutic angiogenesis has emerged as a promising strategy for restoring microcirculation [14–16]. This approach enhances neovascularization within ischemic tissues, supports collateral vessel formation, and improves tissue perfusion. Among the strategies examined, the direct delivery of proangiogenic proteins or mesenchymal stem cells (MSCs) into ischemic sites has been extensively investigated [17–21]. Numerous preclinical studies have demonstrated that appropriate doses of bioactive factors or cells can restore perfusion, and several clinical trials are currently underway [22–24]. Among the MSC subtypes, adipose-derived stem cells (ADSCs) are widely utilized in ischemic disease treatment owing to their strong secretion of proangiogenic factors and ease of isolation [25]. Studies further indicate that delivering MSCs as spheroids rather than as single-cell suspensions enhances their survival and function performance in vivo [26–28]. However, injection-based therapies face numerous challenges: injected cells can be displaced by blood flow, causing off-target effects, while therapeutic responses often vary considerably among patients, complicating treatment outcome standardization [29]. To address these challenges, hydrogel-based delivery systems using materials such as collagen and fibrin have been developed for localized delivery of therapeutic factors or stem cells [30–32]. These hydrogels possess tissue-mimetic mechanical properties, thereby enabling stable adhesion to target sites and providing an extracellular matrix (ECM)-like environment that supports cell survival and function [30]. Recently, prevascularized implants incorporating endothelial cells (ECs) into hydrogel matrices have been engineered for ischemic therapy [33–37]. Implanted grafts containing pre-induced capillaries have been shown in various in vivo studies to integrate with host vessels and progressively develop into functional vascular networks [34, 38–41]. These prevascularized structures, capable of vascular integration, have been associated with accelerated perfusion recovery and reduced tissue necrosis compared to conventional implants [35–37]. However, the majority of prevascularized grafts are limited to forming microvascular structures and lack sufficient paracrine activity to drive functional therapeutic angiogenesis. In our previous work, we showed that the design of prevascularized patterns influences graft vascularization. In particular, combining two distinct spatial patterns—pre-induced capillary networks positioned adjacent to angiogenic factor–secreting cell regions—enhanced in vivo neovascularization compared to capillary-only constructs [40]. In a separate study, we also found that spatially patterned MSC spheroids promote host vessel infiltration and improve graft integration through localized paracrine signaling [42]. While these findings suggest that spatial control over angiogenic factor–secreting components is important for neovascularization, they were examined independently and in non-ischemic contexts, which do not fully capture the impaired vascular environment of ischemic tissues. Therefore, we hypothesized that integrating pre-induced microvascular networks with spatially organized MSC spheroids within a single construct could synergistically enhance vascularization by providing both structural guidance for vascular integration and localized proangiogenic signaling, with potential to improve therapeutic angiogenesis in ischemic tissues.

In this study, we developed a dual-function prevascularized graft aimed to enhance angiogenesis for treating ischemic diseases (Fig. 1). The implantable graft was fabricated

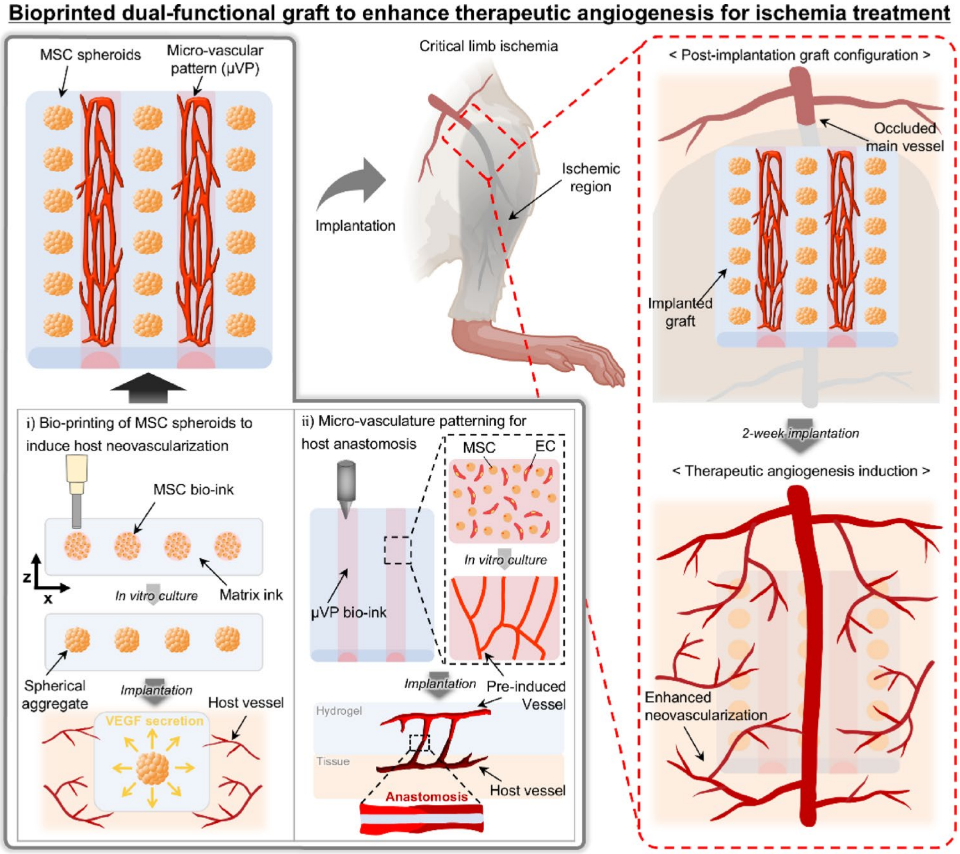

Fig. 1 Schematic illustration of a dual-functional prevascularized graft designed to enhance therapeutic angiogenesis in ischemic tissue. The graft was fabricated using bioprinting to integrate spatially organized MSC spheroids and microvascular patterns (μVPs) within a hydrogel matrix. MSC bio-ink and μVP bio-ink were cultured in vitro to form spheroids and pre-induced capillaries, respectively, prior to implantation. Upon implantation into ischemic tissue, the graft promotes host neovascularization through VEGF secretion and facilitates vascular anastomosis via pre-induced capillaries, ultimately enhancing therapeutic angiogenesis

by bioprinting MSC spheroids and EC-based microvascular patterns (μVPs), thereby offering complementary functions for ischemic tissue regeneration. The MSC spheroids were embedded within a printed matrix ink to provide sustained angiogenic factor secretion, thereby promoting host vessel neovascularization. Simultaneously, predefined μVP were bioprinted across the graft and pre-induced into high-density capillaries prior to implantation, promoting anastomosis with host vasculature and enabling rapid blood flow restoration. The graft design was systematically optimized to enhance the functionality and maturation of each bioprinted component, thereby supporting effective neovascularization in vivo. To evaluate the synergistic therapeutic effect of combining MSC spheroids with μVP, the graft was applied in a mouse model of critical limb ischemia, while its ability to promote vascular regeneration in ischemic tissues was assessed.

Materials and methods

Cell culture

Human ADSCs (Lonza, Basel, Switzerland), employed as the MSC source in this study, were cultured in HyClone^{TM} Dulbecco's Modified Eagle Medium with low glucose (Cytiva, Marlborough, MA, USA) supplemented with 10% fetal bovine serum (FBS; Gibco, Marcq-en-Baroeul, France) and 1% penicillin/streptomycin (Gibco) and maintained up to passage 8. Green fluorescent protein (GFP)-expressing human umbilical vein endothelial cells (Angio-Proteomie, Boston, MA, USA) were cultured in EGM-2 (Lonza) medium up to passage 7. Culture medium for both cells was replaced every 2 days, while cells were subcultured every 3 days using 0.05% trypsin-EDTA (Gibco).

Preparation of printing inks

Three types of printing inks—matrix ink, MSC bio-ink, and μVP bio-ink—were utilized in this study, with their compositions based on our previous studies [40, 42]. Detailed formulations are presented in Tables S1 and S2. All bio-inks were prepared by dissolving the hydrogels using a rotator. Regarding the matrix ink, hyaluronic acid HA (Sigma-Aldrich, Darmstadt, Germany) was dissolved in calcium- and magnesium-free minimum essential medium (MEM; ATCC, Manassas, VA, USA) overnight. The following day, additional components were simultaneously added and incubated at 37 °C as follows: alginate (PRONOVA UP MVG; NovaMatrix, Norway) for 2 h, fibrinogen (F8630;

Sigma-Aldrich) for 1 h, and gelatin (G6144; Sigma-Aldrich) for 30 min. For the MSC bio-ink, HA was dissolved in MEM overnight, followed by pluronic-127 (9003-11-6, Sigma-Aldrich) at 4 °C. Gelatin was dissolved for 30 min at 37 °C, while $CaCl_2$ (Junsei Chemical, Tokyo, Japan) was added. As regards the µVP bio-ink, HA was dissolved in MEM overnight at 37 °C, followed by fibrinogen for 1 h and gelatin for 30 min. All bio-inks were then sterilized by filtration using a 0.45 µm syringe filter. Prior to bioprinting, detached cells (MSCs and ECs) were homogeneously mixed with their respective bioinks. Cell concentrations were determined based on our previous studies to ensure stable capillary and cell-aggregate formation [40, 42]. Finally, all bio-inks were loaded into 1 mL tuberculin syringes for the printing.

3D bioprinting process

The custom-built bioprinter, described in a previous study [40], was used for all experiments. The printer comprised a three-axis stage, numerous dispensing modules, and an enclosure equipped with a temperature controller, UV lamp, HEPA filter, and humidifier. Printing was conducted at 18 °C with humidity above 70%. An in-house software generated printing paths based on the construct design. Printing procedures varied by experimental group: First, a polycaprolactone (PCL; Polysciences, Inc., Warrington, PA, USA) frame was printed and filled with matrix ink. The µVP bio-ink was deposited linearly, while the MSC bio-ink was printed in dot form. PCL was printed using a metal nozzle (200 µm diameter) at 90 °C and 280 kPa. Metal nozzles with diameters of 300 and 200 µm were used to print the matrix ink and µVP bio-inks, respectively. For dot-printing MSC spheroids, a metal needle nozzle (120 µm diameter and 6.5 mm length) with dispensing times of 3, 6, or 9 s were utilized. Printed constructs were crosslinked by treatment with 40 mM $CaCl_2$ and 5U/mL thrombin for 30 min to stabilize the alginate and fibrinogen in the matrix ink. After adding culture media, constructs were incubated at 37 °C in a CO_2 incubator. Constructs containing only MSC patterns were cultured in low-glucose DMEM supplemented with 10% FBS and 1% P/S, while those with µVP designs, including EC, were cultured in EGM-2.

Measurement of mechanical properties of printing inks

To analyze the shear-thinning properties and measure the viscosity of the matrix inks, shear sweep analysis was performed using a modular compact rheometer (Anton Paar MCR102; Anton Paar, GmbH, Austria). After the thermal-crosslinking of gelatin at 4 °C for 10 min, measurements were conducted at 0.1–100 s^{-1} using a plate with a diameter of 20 mm. The viscoelastic properties of the matrix ink and µVP bio-ink were further evaluated by measuring the storage modulus (G′) and loss modulus (G″) through dynamic frequency sweep analyses using the same rheometer. Measurements were performed over a frequency range of 0.05–100 Hz at room temperature after the crosslinking. The compressive moduli (mechanical stiffnesses) of the ionically and enzymatically crosslinked matrix inks were measured using an Instron Model 3342 universal testing machine (Illinois Tool Works Inc., Massachusetts, USA). Disks (5 mm diameter) were prepared for each of the four matrix ink compositions: (i) A12 (control), (ii) A12F10, (iii) A8F10, and (iv) A4F10 (Table S1). Under controlled conditions, each specimen was compressed at a rate of 1 mm/min, while force-displacement data were recorded. The stress−strain curves were plotted, and the slope in the initial 10% strain region used to determine the compressive modulus.

Quantitative analysis of spheroid diameter, sprouting, capillary formation, and cell viability

Printed constructs were observed using an inverted bright-field microscope (Leica DMI-1; Leica Microsystems, Hamburg, Germany) and a fluorescence microscope (DM2500; Leica Microsystems) for general imaging. Detailed z-stacked 3D images were acquired using a confocal laser scanning microscope (FV1000; Olympus, Tokyo, Japan). Spheroid regions were identified as high-density cell clusters in bright-field images, while their diameters were measured manually during the culture period. Sprout length was denoted as the distance from the spheroid edge to the tip of each extension. Capillary formation within printed µVP construct was quantified using AngioTool software (National Cancer Institute, Bethesda MD, USA) to measure the vessel area coverage (%) and average vessel length (µm).

Cell viability was assessed using a Live/Dead Viability/Cytotoxicity kit (L3224; Invitrogen). Constructs were washed with Dulbecco’s phosphate-buffered saline (dPBS) and incubated at room temperature for 30 min in a staining solution containing 0.5 µL/mL calcein-AM and 2 µL/mL ethidium homodimer in dPBS. Stained constructs were imaged using a confocal microscope (FV1000; Olympus), while dead cell density was calculated as the number of dead cells divided by the area occupied by live cells using ImageJ software (National Institutes of Health, Bethesda, MD, USA).

Analysis of vascular endothelial growth factor (VEGF) secretion of printed MSC spheroids

Constructs were cultured for 4 days, while conditioned media were collected on days 2 and 4. VEGF concentrations in the conditioned medium was determined using an enzyme-linked immunosorbent assay (ELISA) kit designed for Human VEGF (Quantikine ELISA Kit; R&D Systems, Minneapolis, MN, USA). To enable accurate comparisons, VEGF levels were normalized to ATP content, quantified using the CellTiter-Glo® 3D cell viability assay (Promega, Madison, WI, USA).

Immunocytochemistry

Constructs were fixed in 4% paraformaldehyde (Junsei) at 4 °C overnight, followed by washing in saline containing 2.5 mM $CaCl_2$ at 4 °C for 2 days. Samples were then permeabilized with 0.1% Triton X-100 for 1 h at room temperature (RT) and blocked with 5% bovine serum albumin (Sigma) for 3 h at RT to prevent nonspecific antibody binding. Primary antibodies were applied for 48 h at 4 °C: rabbit anti-CD44 (Proteintech, Chicago, IL, USA, Cat# 15675-1-AP, 1:100 dilution) and rabbit anti-SOX2 (Abcam, ab92494, 1:100 dilution. After incubation, constructs were washed overnight in PBS at 4 °C and then incubated with the secondary antibody, Alexa Fluor 568-conjugated goat anti-rabbit IgG (Invitrogen, Cat# A-11036, 1:1000 dilution), for 2 h at RT. Nuclei were stained with 4′,6-diamidino-2-phenylindole (DAPI; Vector Laboratories, Burlingame, CA, USA; 1:1000 dilution) for 30 min at RT. Stained constructs were imaged using a confocal microscope (FV1000, Olympus).

Animal studies

All animal experiments were conducted in accordance with institutional guidelines and approved by the Institutional Animal Care and Use Committee (IACUC) of UNIST (UNIST-IACUC-23-39) and Pusan National University (PNU-2026-0751). BALB/c nude mice (Orient Bio, Republic of Korea) were used for all in vivo studies, with sex and age specified for each experimental model as described in the corresponding sections.

Subcutaneous implantation model

To evaluate neovascularization and host vessel infiltration, printed constructs ($8 \times 8 \times 1$ mm^3) were cultured for 6 days prior to implantation. Eight-week-old male BALB/c nude mice were anesthetized with isoflurane, and a dorsal skin incision was made to implant the constructs into the subcutaneous space. Incisions were closed using 6–0 prolene sutures (Ethicon, Somerville, NJ, USA). Grafts were harvested after 1 or 2 weeks by careful dissection from the surrounding skin and muscle. The harvested grafts were imaged using a Dino-Lite digital microscope (AM4113T, AnMo Electronics, New Taipei City, Taiwan) and then fixed with 4% paraformaldehyde for subsequent immunohistochemical analysis.

Cutaneous wound healing model

Six-week-old male BALB/c nude mice (18–22 g) were used. Anesthesia was induced by intraperitoneal injection of Avertin (2,2,2-tribromoethanol, Sigma-Aldrich) at a dose of 400 mg/kg. A full-thickness square excisional wound matching the dimensions of the printed constructs was created on the dorsal skin of each mouse.

Five different printed constructs were prepared using the same parametric designs and culture conditions as those in the subcutaneous implantation model. To match the total number of mesenchymal stem cells (MSCs) between the Cell-mixed Gel and Spheroid Only groups, the MSC concentration in the Cell-mixed Gel group was determined based on the number of spheroids, the estimated cell density per spheroid, and the construct volume. Specifically, the concentration was calculated as $(16 \times 1 \times 10^8 \times 3.9 \times 10^{-5})$ / $(8 \times 8 \times 1$ mm$^3)$, resulting in a final concentration of approximately 0.98×10^6 cells/mL, corresponding to $\sim 1 \times 10^6$ cells/mL. Prior to implantation, the PCL frame was removed to avoid interference with wound closure. On day 0, constructs corresponding to each experimental group were implanted into the wound sites. The wounds were then covered with a transparent dressing film to prevent dehydration and minimize disturbance. Wound healing progression was monitored by photographing the wound area at predetermined time points. Wound areas were quantified using ImageJ and normalized to the initial wound size to calculate the percentage of wound closure over time.

In vivo blood perfusion measurement using Doppler flow imaging

Blood perfusion at the wound sites during the healing process was assessed using a laser Doppler flow imaging system (MoorLDI2-HR, Moor Instruments, UK). All measurements were performed under controlled environmental conditions at an ambient temperature of 26 °C. The imaging head was positioned approximately 35 cm above the anesthetized mice to enable scanning of the wound area together with the adjacent inter-wound regions.

The laser Doppler perfusion imaging (LDPI) index, which reflects the level of blood flow within the tissue, was quantified using Moor LDI v5.3D software (Moor Instruments, Inc.). For each measurement, the wound region and surrounding inter-wound areas were scanned, generating a blood perfusion image. To obtain the LDPI index per unit area, the wound region and a 6-mm-wide section extending from the midpoint of the inter-wound region were selected and analyzed. The obtained LDPI values were normalized against those measured from intact skin. LDPI images were acquired on days 6 and 9 following wound induction. Blood perfusion was visualized using a color-coded scale, where red indicated high perfusion and blue represented low perfusion. The LDPI index was used as a quantitative indicator of blood flow within the wound region, enabling comparison of perfusion dynamics during the wound-healing process.

Hindlimb ischemia model

A critical limb ischemia model was established based on a previous protocol [43]. Six-week-old female BALB/c nude mice (Orient Bio) were anesthetized, and incisions made on the left limbs. Electrocauterization was performed at two points between the left iliac and femoral arteries to completely excising the main vessel bundles, thereby accommodating the printed construct size ($6 \times 8 \times 1\ \mathrm{mm}^3$). Prior to implantation, the PCL frame of the printed graft was carefully removed to prevent tissue damage caused by sharp edges. The grafts were placed on the exposed muscle tissue in the vessel-resected area, while incisions were closed using 6–0 prolene sutures (Ethicon) to maintain proper implant positioning. On days 3, 7, and 14, the physiological status of the left lower limb was evaluated using a scoring system. Limb loss was recorded in cases of lower-extremity amputation, while deteriorating skin and muscle, darkened nails, and cyanotic skin indicated foot loss. Preserved limb without complications were considered salvaged. Two weeks after implantation, mice were euthanized and sacrificed for immunohistochemical and histological analyses. To analyze the therapeutic effects and vascular regeneration of the implanted grafts, tissue samples were harvested from the quadriceps muscle at the implantation site, distal to the electrocauterization site. This region enables direct assessment of local therapeutic effects and allows for consistent analysis across all experimental groups.

Histological analysis and immunohistochemistry

The harvested ischemic muscles were fixed in 4% paraformaldehyde (Junsei) at 4 °C overnight, followed by washing in PBS at 4 °C overnight. Tissues were processed, paraffin-embedded, and sectioned into 8 μm-thick slices using a microtome. For histological analysis, sections were stained with hematoxylin and eosin (H&E), picrosirius red (PSR) and Masson's trichrome (MT). For immunohistochemistry, sections were stained with Alexa Fluor 647 anti-mouse CD31 (BioLegend, California, USA, Cat# 102416, 1:100 dilution), rabbit anti-α-SMA (Abcam, Cat# ab5694, 1:100 dilution), and rabbit anti-GFP (Abcam, Cat# ab6556, 1:100 dilution) antibodies, with PBS used for washing. The secondary antibody was then added by incubation with Alexa Fluor 488-conjugated goat anti-rabbit IgG (Invitrogen, Cat# A-11008, 1:1000 dilution) for 2 h at RT. Nuclei were counterstained with DAPI for 5 min at RT, and sections were imaged using a confocal microscope (FV1000, Olympus). Immunostained sections were examined under a fluorescence microscope (DM2500; Leica Microsystems) and confocal microscopes (FV1000, Olympus; LSM780, Zeiss Oberkochen, Germany). For bright-field-based histological analysis, H&E- and MT-stained sections were imaged using a dotSlide digital virtual microscope (BX51/22, Olympus, Tokyo, Japan), and PSR images were acquired under polarized light using a THUNDER imaging system (Leica Microsystems). To quantitatively investigate neovascularization among experimental groups, at least two images per animal were analyzed using ImageJ (National Institutes of Health). The numbers of capillaries and arterioles were manually counted based on CD31- and α-SMA-positive vessel-like structures showing clear lumens. Capillary density was quantified as the CD31-positive area divided by the total image area. Vessel and arteriole sizes were determined by measuring the area of CD31- and α-SMA-positive vessel-like structures with clear lumens. For statistical analysis, measurements from multiple images of the same animal were averaged to obtain a single representative value per animal, and all comparisons were performed using biological replicates (independent animals).

Statistical analysis

Data collected in this study are presented as the mean ± standard deviation. Statistical analyses were conducted using Origin Pro 2020 (OriginLab Corporation, Northampton, MA, USA). Unpaired Student's t-tests and one- or two-way analysis of variance (ANOVA) were applied as appropriate statistical tests based on the experimental design. Statistical significance was denoted as $^{*}p < 0.05$, $^{**}p < 0.01$, $^{***}p < 0.001$, and $^{****}p < 0.0001$.

Results and discussion

Fabrication of MSC spheroids with enhanced VEGF secretion via in-bath bioprinting

To promote enhanced therapeutic angiogenesis, we developed an in-bath bioprinting process to fabricate MSC spheroids with high angiogenic factor secretion at predefined locations. We previously developed a spheroid bioprinting technique that utilizes alginate as a matrix ink and a calcium-containing cell bioink to entrap the printed bioink within the surrounding matrix ink [42, 44]. Based on this technique, in this study, we prepared an alginate-fibrinogen-based matrix ink containing RGD-binding sites and a gelatin-based MSC bioink, specifically using ADSCs, at high cell density (100 million cells/mL). The effects of varying in-bath printing parameters on MSC spheroid formation and VEGF secretion were systematically evaluated (Fig. 2A). First, we evaluated how alginate and fibrinogen concentrations in the matrix ink influenced printability and spheroid integrity. Post-printing morphology was examined microscopically to identify printable versus nonprintable conditions (Fig. 2B and C). Consistent spherical morphologies were observed when the matrix ink had an appropriate composition (Fig. 2B, top image). However, at low alginate and fibrinogen concentrations, MSC bioinks failed to maintain spherical shapes, while excessively high concentrations

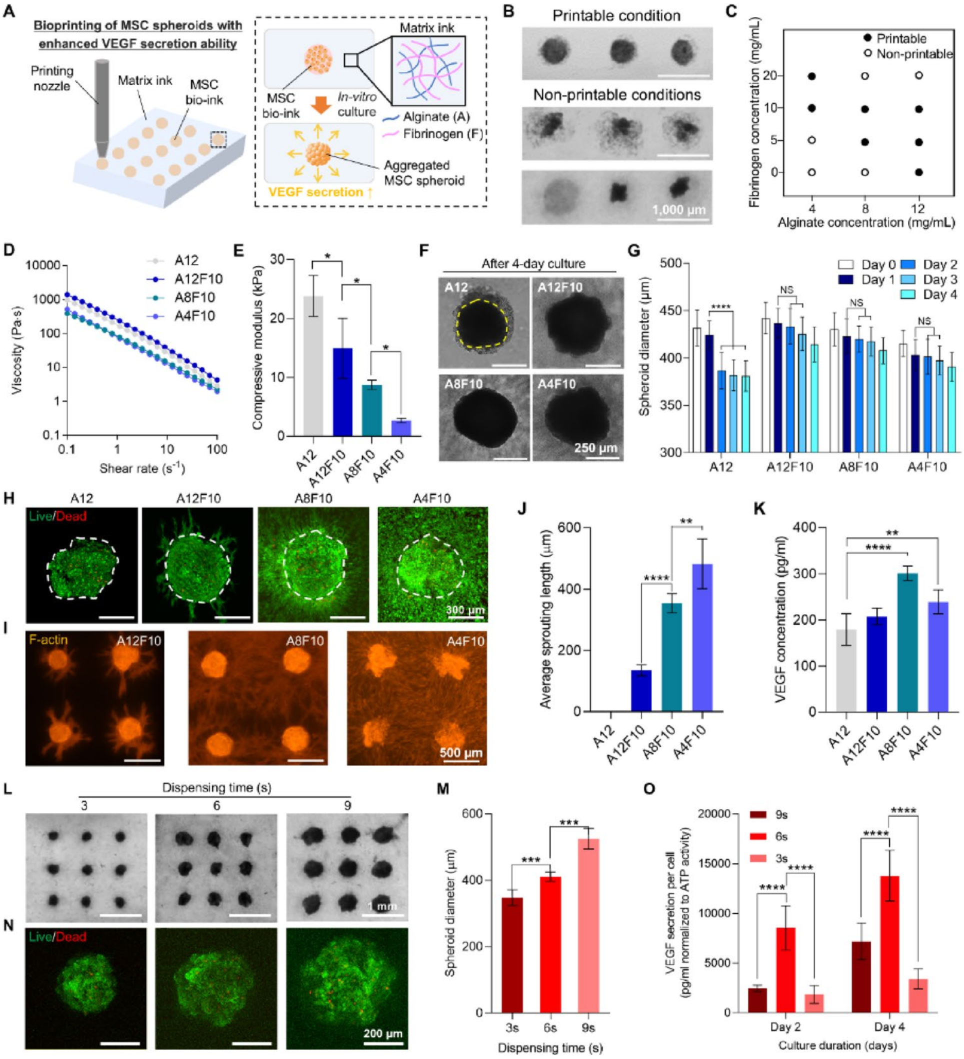

Fig. 2 Optimization of bio-ink compositions and printing conditions to enhance VEGF secretion from bioprinted MSC spheroids. **A** Schematic illustration of the bioprinting process and induction of MSC spheroids. (**B**) Printability graphs of matrix ink showing printable and non-printable results based on varying concentrations of alginate **A** and fibrinogen **F**. **D** Rheological characterization showing the viscosity of uncrosslinked matrix inks with different compositions ($n=4$). A12, A8, and A4 denote alginate concentrations of 12, 8, and 4 mg/mL, respectively, and F10 indicates a fibrinogen concentration of 10 mg/mL **E** Compressive modulus of crosslinked matrix ($n=10$). **F** Bright-field images showing morphological differences of printed MSC spheroids in different matrix inks at day 4 post-printing. Yellow dashed lines indicate the aggregate morphology of MSC spheroids in A12 matrix ink. **G** Quantification of spheroid diameters after printing ($n=30$). **H** Representative confocal z-stacked images of bioprinted MSC spheroids stained with calcein (green, live cells) and ethidium homodimer (red, dead cells) at day 4 post-printing. **I** Fluorescence images of F-actin stained MSC spheroids showing the sprouted morphologies of MSCs on day 4. **J** Quantification of average sprouting lengths of MSC spheroids in different matrix inks ($n=6$). **K** VEGF secretion levels of MSC spheroids ($n=6$). **L** Bright-field images showing MSC spheroids with different dispensing times. **M** Measured diameters of the bioprinted MSC spheroids according to different dispensing times on day 4 ($n=16$). **N** Representative confocal z-stacked images showing the viability of MSC spheroids. **O** Quantification of VEGF concentrations normalized to ATP activity (measured in relative luminescence units; 10^6 RLU) ($n=6$). NS, not significant. *$p<0.05$, **$p<0.01$, ***$p<0.001$, ****$p<0.0001$

resulted in irregular structures (Fig. 2B, bottom two images). Based on the printable conditions identified in Fig. 2C, four matrix ink formulations—A12, A12F10, A8F10, and A4F10—were selected for further experiments. These conditions were chosen by fixing the fibrinogen concentration to provide a consistent RGD-binding environment while varying the alginate concentration to assess spheroid formation during the culture period. Here, "A" and "F" denote alginate and fibrinogen concentrations (mg/mL), respectively. To further elucidate the printability of the selected matrix inks, rheological analysis demonstrated shear-thinning behavior in all formulations, with A12F10 exhibiting the highest viscosity (Fig. 2D).The mechanical properties of the cross-linked matrix inks were measured under each condition. As the alginate concentration increased, the compressive modulus increased, with A12 exhibiting the highest modulus among the groups (Fig. 2E). Although A12F10 contained additional fibrinogen, its modulus was lower than that of A12. This result corresponds with previous reports indicating that fibrinogen incorporation can soften alginate-based hydrogels, thereby disrupting the formation or compaction of ionically crosslinked network [45–47]. Interestingly, A12 exhibited the highest compressive modulus, while A4F10 showed a significantly lower modulus, whereas A12F10 and A8F10 exhibited values closer to that of native skeletal muscle (~ 10–17 kPa) [48, 49], indicating a more favorable mechanical environment for implantation in ischemic tissues. After bioprinting under these conditions, the aggregation behavior of printed MSCs was observed during culture using bright-field microscopy. At day 4, the A12 group showed a noticeable reduction in spheroid size compared with other groups (Fig. 2F). Quantitative analysis confirmed that spheroid diameters decreased over time in all groups, although the reduction was more prominent in the A12 condition (Fig. 2G). The A12 group exhibited a rapid decrease in diameter by day 2, while the other groups exhibited more gradual compaction. Live/dead staining on day 4 confirmed high cell viability across all groups, with noticeable cell migration at the periphery of spheroids, particularly in fibrinogen-containing matrix inks (Fig. 2H). F-actin staining further revealed the elongated morphology of migrating cells surrounding the spheroids (Fig. 2I). Quantitative analyses indicated that lower alginate concentrations promoted longer sprout formation, with the A4F10 group exhibiting the longest sprouts (Fig. 2J). Immunostaining analysis showed that stemness-associated markers (CD44 and SOX2)were consistently expressed across matrix compositions (Fig. S1), suggesting maintenance of a stem-like phenotype without apparent differentiation during culture. VEGF secretion analysis revealed that lower alginate concentrations and the inclusion of fibrinogen enhanced VEGF release from MSC spheroids (Fig. 2K). These findings suggest that the inclusion of fibrinogen, which is known to provide RGD-binding sites, facilitates cell migration and enhances angiogenic factor secretion. These observations are also consistent with previous reports demonstrating that stem-like phenotypes are associated with increased secretion of angiogenic factors in softer hydrogel environments [50–53]. A positive correlation was observed between active cellular sprouting and VEGF secretion. However, the A4F10 group secreted less VEGF than the A8F10 group despite extensive cell migration owing to inadequate stable spheroid formation (Fig. 2I). These results suggest that a balanced matrix mechanical property contributes to stabilizing MSC spheroids while supporting functional sprouting and angiogenic factor secretion. Based on these findings, A8F10 was identified as the optimal matrix ink formulation for maximal VEGF secretion, which was selected for subsequent studies.

Hypoxic conditions within stem cell spheroids considerably influence growth factor secretion [27]. This arises from the limited diffusion of oxygen and nutrients into the core of larger spheroids, creating a hypoxic environment that drives the upregulation of proangiogenic factors. Hence, spheroid diameter serves as a key determinant of angiogenic factor production. To assess this effect, MSC spheroids were printed using dispensing times of 3, 6, and 9 s, while their size and function were evaluated (Fig. 2L). Increasing dispensing time resulted in an increase in spheroid diameter, resulting in spheroids ranging from approximately 350–520 μm after 4 days of culture (Fig. 2M). Live/dead staining demonstrated high overall viability, though larger spheroids contained a higher density of dead cells (Fig. 2N), which corresponds with quantitative analyses (Fig. S2A). ATP measurements on day 4 showed that MSC spheroids printed at 6 s exhibited the highest metabolic activity, while those printed at 9 s exhibited the lowest (Fig. S2B). The reduced viability in larger spheroids may be attributed to severe hypoxic [54, 55]. Hypoxia, in turn, enhances angiogenic factor secretion [27]. VEGF secretion per cell, normalized to ATP activity, was highest at 6 s, followed by 3 and 9 s (Fig. 2O). While previous reports using microwell-based spheroid fabrication have shown enhanced VEGF secretion in spheroids with diameters ranging from 150 to 250 μm [54–58], in our system the highest VEGF secretion was observed at approximately 400 μm. This discrepancy may be attributed to variations in the hypoxic microenvironments arising from the RGD-binding matrix (fibrinogen) and mild compaction process utilized herein, which differs from conventional microwell-based spheroid fabrication (Fig. 2F). In conclusion, MSC spheroids printed at 6 s in fibrinogen-containing matrix ink exhibited the highest VEGF secretion and were selected for subsequent experiments.

Spatial influence of MSC spheroids on capillary formation within µVPs

To determine optimal conditions for fabricating prevascularized grafts with enhanced capillary formation, linear µVPs were printed using a fibrinogen-based bio-ink containing ECs and MSCs, following formulations established in our previous study [40]. MSC spheroids were simultaneously printed at three distances (250, 500, and 1,000 µm) from the µVP (Fig. 3A and B). Vasculogenesis-like responses of ECs within the µVPs were monitored over time. By day 2, ECs clustered along the central axis of the µVPs across all groups (Fig. 3C). By day 6, closer proximity between the µVPs and MSC spheroids resulted in more robust and denser capillary formation. Quantitative analysis confirmed these trends, with vessel area coverage and length considerably increasing as the spheroid-to-µVP distance decreased (Fig. 3D and E).

To assess endothelial junction formation, immunostaining for the tight junction marker Zonula Occludens-1 (ZO-1) was performed. Elongated ZO-1-positive vessel walls were observed in all the groups, indicating the formation of endothelial junctions (Fig. S3). Although signal intensities were similar across groups, capillary density varied with spheroid-to-µVP distance. Additionally, MSCs within the µVP exhibited α-smooth muscle actin (α-SMA) and neural/glial antigen 2 (NG2) positivity, suggesting they acted as pericyte-like supporting cells contributing to vessel stabilization (Fig. S4) [59, 60]. To evaluate endothelial junction and angiogenesis-related gene expression influenced by EC-MSC spheroid interactions, quantitative reverse transcription-polymerase chain reaction (qRT-PCR) was performed. Among the groups, the 250-µm distance group exhibited the highest expression of endothelial junction-associated markers (Fig. 3F), with statistically significant upregulation of ZO-1 and Claudin-5. A similar trend was observed for angiogenesis-associated markers, including Angiopoietin-1 (ANGPT1) and VEGF. These results are consistent with enhanced endothelial organization and angiogenic activity at shorter distances, likely mediated by increased paracrine interactions [61]. Constructs cultured for up to 10 days exhibited no further increase in vascular density or vessel length beyond day 6 (data not shown). Based on these results, a 250-µm spheroid-to-µVP distance was identified as an optimal condition for prevascularized graft fabrication, yielding enhanced capillary formation and endothelial organization.

Hydrogel systems coencapsulating ECs and MSCs have been widely investigated as a prevascularization strategy to promote microvascular structure formation [35, 41, 59–62]. Beyond stimulating EC angiogenic responses, MSCs can act as pericyte-like supporting cells when in direct contact with ECs within hydrogels, thereby contributing to vascular stabilization [59, 60]. Pre-formed capillaries co-cultured with MSCs within hydrogels have shown promising outcomes in vessel regeneration following implantation in various animal models [35, 41, 59, 62]. In our previous study, we also demonstrated that the formation of stable microvascular structures within µVPs comprising MSCs and ECs promoted graft vascularization in vivo [40]. Further, we observed that the designed grafts incorporating both MSC patterns and µVPs enabled a more spatially defined angiogenic factor gradient, resulting in enhanced vascularization compared to grafts containing µVPs alone. Based

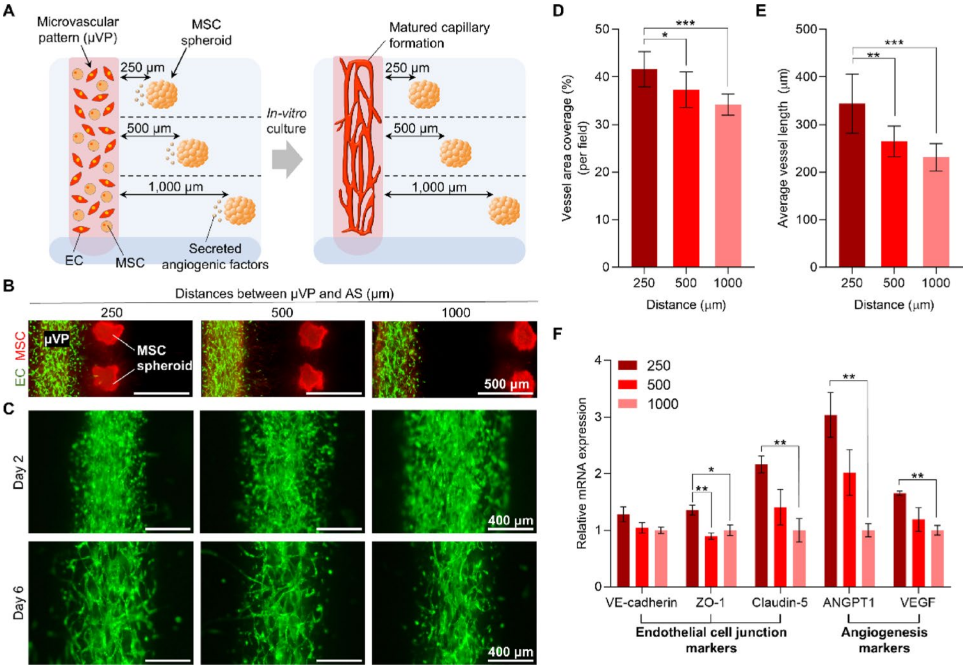

Fig. 3 Investigation of capillary formation within microvascular patterns (µVPs) based on the distance from MSC spheroids. **A** Schematic illustration of bioprinted constructs with varying distances (250, 500, or 1,000 µm) between µVP and MSC spheroids to investigate capillary formation. **B**, **C** Fluorescent images showing bioprinted µVP and MSC spheroids at different distances, and a magnified view of µVP on days 2 and 6 post-printing. **D**, **E** Quantification of vessel area coverage ($n=8$) and average vessel length ($n=8$) of in vitro formed capillaries within µVPs after 6 days of culture. **F** Gene expression levels of endothelial junction- and angiogenesis-related markers in printed constructs with different distances ($n=4$). $^{*}p<0.05$, $^{**}p<0.01$, and $^{***}p<0.001$

on these findings, we applied precision printing of angiogenic MSC spheroids to fabricate prevascularized grafts, as MSC spheroids have been shown to enhance angiogenic factor secretion for ischemic tissue repair [26–28]. Given their role as localized sources of paracrine signaling, we hypothesized that the spatial relationship between MSC spheroids and µVPs would influence in vitro capillary formation, and observed that reduced spacing promoted more active capillary formation within the printed µVPs (Fig. 3). This result corresponds with a previous study demonstrating that bioprinted MSC-endothelial cell patterns maintained at ~200 µm spatial proximity yielded stronger capillary formation than simply mixing two cell types [61]. Our findings highlight that spatial proximity between MSC spheroids and µVPs enhances capillary formation during a 6-day in vitro culture period. While extended in vitro culture may further promote the development of more mature capillary structures with in vivo-like endothelial phenotypes [41], our primary objective was to leverage MSC spheroids as localized sources of paracrine signaling to enhance neovascularization after implantation. Therefore, we defined the pre-implantation culture period as 6 days, consistent with our previous study [40].

Effect of MSC spheroid number on *in vivo* neovascularization and retention of implanted vascular structures

Transplanting prevascularized grafts promotes in vivo neovascularization and host vessel infiltration, initiating dynamic interactions between host and engineered vasculature that result in functional microvessel [38, 41]. In this study, we investigated how the number of embedded MSC spheroids within prevascularized grafts influenced this process, notably neovascularization and host vessel infiltration. Prevascularized grafts ($8 \times 8 \times 1$ mm^3) containing different spheroid numbers were subcutaneously implanted into the dorsal region of mice (Fig. 4A). The experimental groups were prepared with 0, 8, 16, 24, or 32 spheroids per graft, with MSC spheroids printed in four rows according to the specified numbers and cultured for 6 days prior to implantation to enable µVP and spheroid formation (Fig. S5). Two weeks post-implantation, host vascularization around the explanted grafts exhibited distinct differences among groups (Fig. 4B). In the 0-spheroid group, minimal host vessel formation was detected near the graft. Conversely, grafts containing MSC spheroids—particularly those with 8-, 16-, and 24 spheroids—exhibited dense networks of branching host microvessels that infiltrated the graft. Interestingly, host vessels containing red blood cells infiltrated the graft through the three µVP regions in these groups. To further assess host vessel infiltration into the graft interior, hematoxylin and eosin (H&E) staining was performed (Fig. 4C). The MSC spheroids maintained their aggregated morphology within the matrix ink, with minimal infiltration of surrounding tissue (Fig. 4C, blue box), while numerous vessel-like structures containing red blood cells were observed in the µVP regions (Fig. 4C, red box). This spatial pattern of tissue infiltration between the two printed regions, which share a same fibrinogen composition (Tables S1 and S2), may be attributed to the use of high molecular weight alginate in the matrix ink, which is commonly employed for cell encapsulation due to its ability to permit molecular diffusion while limiting cellular infiltration [63, 64]. Consistent with this, our rheological analysis revealed that the matrix ink exhibited a higher storage modulus, whereas the µVP bioink were significantly softer (Fig. S6), thereby creating a selective microenvironment that facilitates host tissue infiltration into the µVP regions while maintaining MSC spheroids for the sustained release of angiogenic factors. The presence and morphology of these vascular structures within µVP regions varied with spheroid density (Fig. 4D). Notably, grafts without spheroids exhibited few or no microvessels, while the 8-, 16-, and 24-spheroid groups exhibited multiple vessel-like structures with relatively large diameters. Contrarily, the 32-spheroid group primarily exhibited smaller capillary-like structures.

To examine the microvascular structures within the µVP, immunohistochemical staining for CD31 and α-SMA was conducted (Fig. 4E). Consistent with the H&E results, few CD31-positive capillaries were observed in the 0-spheroid group, while the 16- and 24-spheroid groups exhibited abundant CD31-positive capillaries and α-SMA-positive arterioles. In the 32-spheroid group, the vasculature comprised small-diameter capillaries. Quantitative analyses revealed that the number of capillaries and arterioles increased with an increase in MSC spheroids, reaching a peak at 16 spheroids, but decreased when the spheroid number exceeded this level (Fig. 4F and G). A similar trend was observed in the vessel diameter, with the 16-spheroid group exhibiting the largest mean diameter and widest diameter distribution (Fig. 4H). These findings indicate that incorporating 16 to 24 spheroids results in the most extensive neovascularization and host vessel infiltration within the µVP regions of the implanted grafts. Although previous studies have applied direct injection of MSC spheroids to enhance in vivo neovascularization [54–57], the influence of the spheroid number on host neovascularization has, to the best of our knowledge, not been systematically investigated. Further, these approaches often lack spatial control, thereby complicating the evaluation of spheroid numbers owing to spheroid migration and heterogeneous retention within the graft. Conversely, our approach allows precise spatial placement of MSC spheroids within the graft, enabling

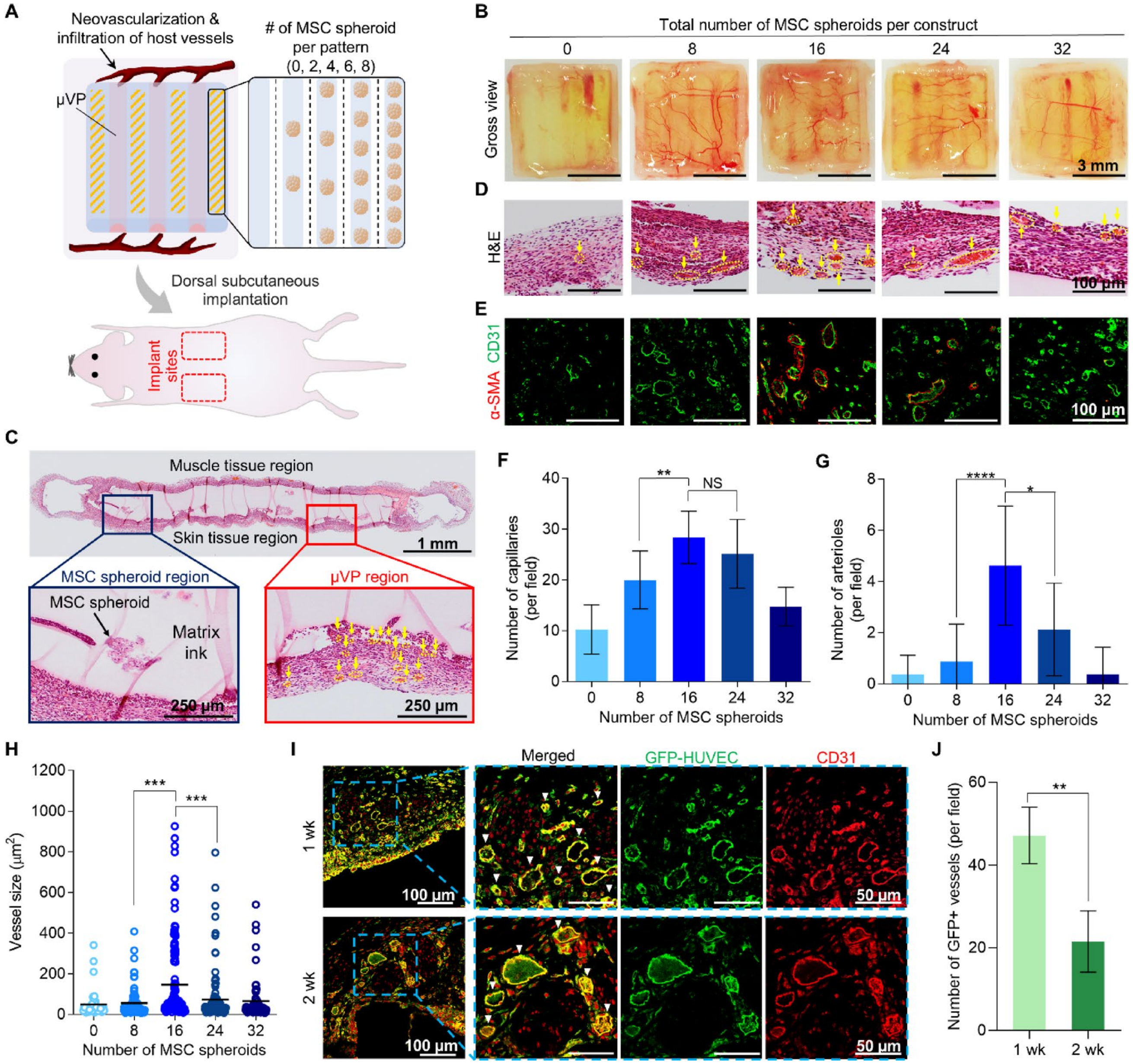

Fig. 4 In vivo effects of prevascularized grafts on neovascularization and retention of implanted vessels in a subcutaneous implantation model. **A** Schematic depicting the experimental design to investigate the inducive effect of host vessel infiltration by varying the number of MSC spheroid per pattern. **B** Gross images of harvested constructs after 2 weeks of implantation. **C** H&E-stained image of whole harvested grafts at 2 weeks post-implantation. Blue boxed region indicates a magnified view of the MSC spheroid region, and red boxed region indicates a magnified view of the µVP region. **D** H&E staining results of the implanted graft within µVP regions showing red blood cells-infiltrated vessel structures (yellow arrows). **E** Immunohistochemical images stained with CD31 and α-SMA within µVP regions. **F**–**H** Quantification of CD31-positive capillaries, α-SMA-positive arterioles, and vessel size was performed using $n = 4$ biological replicates (independent animals), with multiple images analyzed per sample. **I** Immunohistochemical images stained with GFP and CD31 to assess the retention of implanted EC-derived vascular structures at 1 and 2 weeks post-implantation. White arrowheads indicate GFP- and CD31-positive vessels with clear lumens. **J** Quantification of GFP+ vessels ($n = 3$ biological replicates, with multiple images analyzed per sample). $*p < 0.05$, $**p < 0.01$, $***p < 0.001$, and $****p < 0.0001$

controlled evaluation of their paracrine effects on neovascularization. The enhanced vascular outcomes observed in the 16- and 24-spheroid groups reflect an optimized balance between proangiogenic factor secretion and the local metabolic demand of the graft microenvironment. Although replicating the in vivo metabolic dynamics of implanted spheroids remains technically challenging, our study on bioprinting adipose tissue grafts with spatially organized MSC spheroids identified an optimal spheroid number for promoting vascularization [42]. These findings indicate that for an 8 × 8 × 1 mm^3 graft, incorporating approximately 16 MSC spheroids per construct yields the most effective in vivo vascularization, thereby balancing vessel density and maturity.

While the effect of spheroid number on in vivo neovascularization was observed, the origin of vessel structures within the µVP regions after implantation remained unclear. To further examine this, prevascularized constructs containing µVP and 16 MSC spheroids were implanted for 1 and 2 weeks, and the harvested grafts were co-immunostained for GFP-labeled ECs and the endothelial marker CD31 (Fig. 4I). At 1 week post-implantation, numerous GFP-positive/CD31-positive vessel structures were detected within the µVP regions, indicating retention of implanted EC-derived capillaries. In addition, small CD31-positive but GFP-negative structures were observed, suggesting that host endothelial cell infiltration had already begun at this stage. By 2 weeks, GFP-positive vessels were still present, but their number was reduced. Several larger GFP-positive vessels contained luminal contents lacking DAPI signal and showing strong autofluorescence in the absence of quenching, likely representing red blood cells (Fig. S7). Similar blood-containing structures were also observed in H&E staining (Fig. 4D), suggesting functional integration between implanted vessels and the host vasculature. Quantification showed that the mean number of GFP-positive vessels decreased from 47.2 at 1 week to 21.5 at 2 weeks (Fig. 4J), indicating dynamic changes in the implanted vascular structures. In addition, the presence of α-SMA-positive vessels and red blood cell–perfused structures supports features associated with vascular maturation (Fig. 4E and S7). Consistent with previous reports, these results may reflect ongoing vascular remodeling involving host vessel infiltration and interaction with implanted structures [38, 39, 41]. Taken together, these results indicate that prevascularized grafts with 16 MSC spheroids promote host vessel infiltration, while retaining implanted EC-derived vascular structures and enabling subsequent vascular integration.

MSC spheroid–embedded prevascularized grafts accelerate wound healing and perfusion recovery in a cutaneous wound healing model

To first examine the therapeutic potential of our prevascularized grafts, we employed a cutaneous wound healing model previously established in our studies [65], which allows monitoring of wound healing and perfusion recovery over time (Fig. 5A). The dorsal skin wound, characterized by a relatively low density of neighboring host vasculature, provides a suitable environment to assess tissue repair and neovascularization [66]. This model was used prior to evaluation in a more severe ischemic environment with compromised blood flow. As illustrated in Fig. 5A, five groups were prepared, including two control groups (Gel Only and Cell-mixed Gel) and three experimental groups (Spheroid Only, µVP Only, and µVP + Spheroid). To isolate the effect of MSC spheroid formation, the Cell-mixed Gel group was designed with a homogeneous distribution of MSCs at a concentration (~ 1 × 10^6 cells/mL) matched to the total cell numbers of the Spheroid Only group. After 6 days of in vitro culture, all constructs were implanted into dorsal cutaneous wounds with consistent dimensions, and the outer frame was removed prior to implantation to avoid interference with wound closure. Wound healing was tracked by measuring wound closure and blood perfusion every 3 days using laser Doppler perfusion imaging (LDPI).

Wound closure progressed in all groups over time, but clear differences emerged by day 9 (Fig. 5B). The µVP + Spheroid group showed nearly complete closure, whereas the control groups remained only partially healed. Quantitative analysis confirmed these differences (Fig. 5C), with the µVP + Spheroid group reaching 71.5% wound coverage, compared to 50.1% and 48.7% in the Spheroid Only and µVP Only groups, respectively. In contrast, the Gel Only and Cell-mixed Gel groups showed limited closure (23.5% and 33.5%). LDPI images at days 6 and 9 showed weak signals in the control groups, mainly confined to the wound periphery, whereas the experimental groups showed stronger signals extending toward the wound center (Fig. 5D). The µVP + Spheroid group showed the highest perfusion recovery. Quantitative analysis further showed that the Cell-mixed Gel group had significantly higher LDPI values than the Gel Only group, while both the Spheroid Only and µVP Only groups showed further increases compared to the control groups. The µVP + Spheroid group exhibited the highest LDPI index among all groups (Fig. 5E). Notably, the implanted constructs gradually lost their original shape and showed clear structural shrinkage over time. In several wound sites from the µVP + spheroid group, the hydrogel structure was barely visible by day 6. This is likely due to the absence of the PCL supporting frame, unlike in the subcutaneous model (Fig. 4), along with the relatively thin thickness (~ 1 mm) of the constructs. Despite this structural change, enhanced wound closure and perfusion recovery were consistently observed in the cell-containing groups, suggesting that the hydrogel primarily acts as a transient microenvironment that supports early tissue regeneration rather than a long-term structural scaffold. Histological findings were consistent with the differences in wound healing. Hematoxylin and eosin (H&E) staining at day 6 showed that the control groups (Gel Only and Cell-mixed Gel) exhibited relatively immature tissue architecture, with loosely organized and irregular tissue formation (Fig. 6A). In contrast, the experimental groups (Spheroid Only, µVP Only,

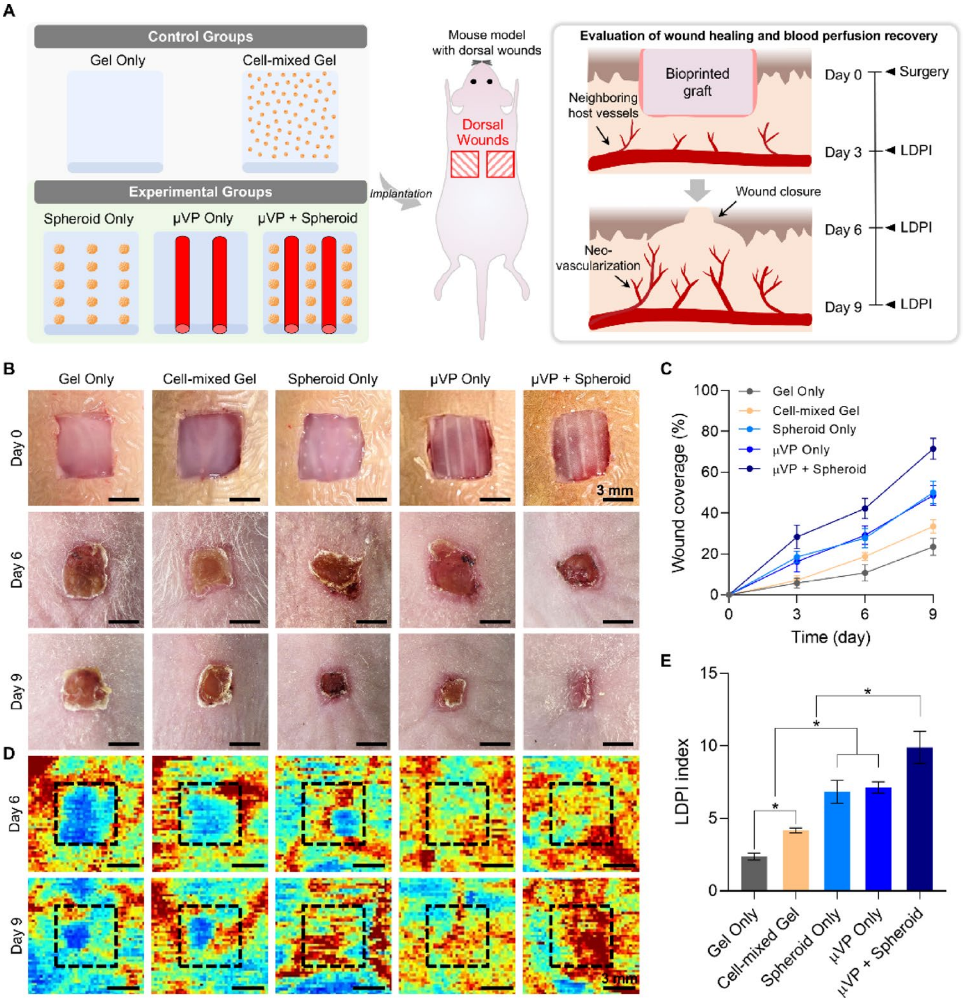

Fig. 5 Investigation of wound healing and blood perfusion recovery in a cutaneous wound healing model. **A** Schematic illustration of the experimental workflow in a mouse dorsal wound model. **B** Representative photographs of wound sites at days 0, 6, and 9 post-implantation. **C** Quantification of wound coverage over time ($n=5$ for days 0–6; $n=2$ for day 9). **D** Laser Doppler perfusion imaging (LDPI) analysis showing blood perfusion at day 6 ($n=5$). $^{*}p<0.05$

and µVP+Spheroid) showed more densely organized tissue, indicating faster healing progression. By day 9, tissue density increased across all groups, with more continuous tissue formation. The µVP+Spheroid group, in particular, showed a clearly defined epidermal layer and improved structural organization, consistent with the macroscopic wound closure (Fig. 5B). Picrosirius red (PSR) staining further revealed differences in collagen deposition among groups (Fig. 6B). At day 6, the µVP+Spheroid group exhibited a more collagen-rich and dense tissue structure, whereas the control groups showed relatively sparse collagen distribution. By day 9, collagen deposition increased in all groups; however, the experimental groups maintained a more densely organized collagen matrix compared to the controls (Fig. S8).

To evaluate neovascularization at the wound site, immunofluorescence staining for CD31 and α-SMA was performed (Fig. 6C). The control groups showed limited CD31-positive capillary formation and minimal α-SMA-positive vessel structures. In contrast, the experimental groups exhibited increased vascularization, with a higher number of CD31-positive capillaries. The µVP+Spheroid group showed the most extensive vascular structures, along with stronger α-SMA-positive signals. Capillary density was higher in all experimental groups than in the Gel Only group, with the µVP+Spheroid group showing the highest density (Fig. 6D). The number of arterioles also increased in the experimental groups, with the µVP+Spheroid group exhibiting the greatest number of α-SMA-positive vessels, suggesting the formation of more mature vascular structures (Fig. 6E). Vessel size did not differ substantially among groups; however, slightly larger vessels were observed in the Spheroid Only and µVP+Spheroid groups compared to the Gel Only group (Fig. 6F). This likely reflects the early stage of angiogenesis at day 9, with vascular sprouting being more prominent than the formation of mature vessels during the proliferative phase of wound healing [67, 68]. Overall, these results show that prevascularized constructs incorporating MSC spheroids promote enhanced wound healing, perfusion recovery, and the neovascularization in the cutaneous wound healing model.

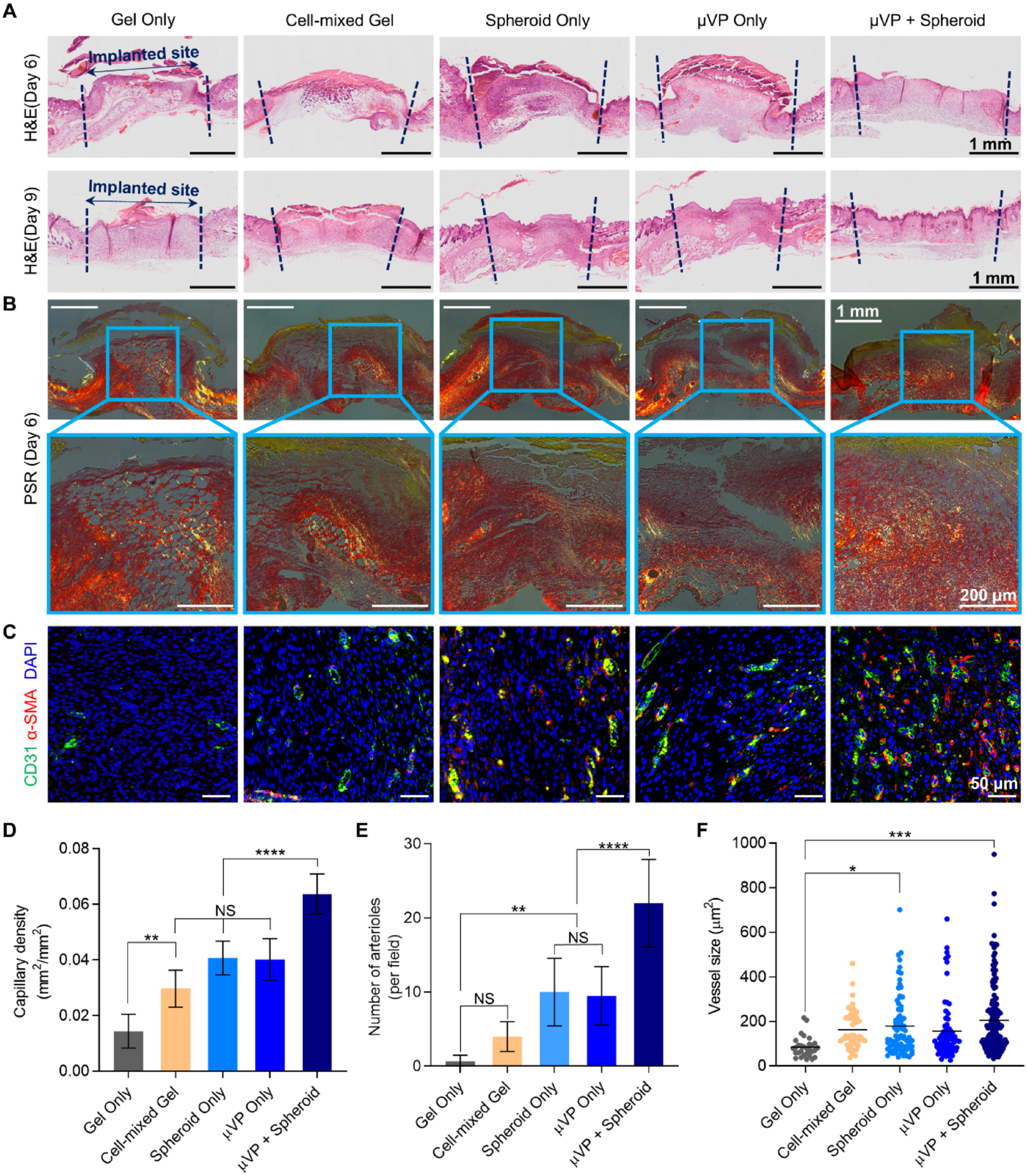

Fig. 6 Histological evaluation of wound healing and vascular regeneration in a cutaneous wound healing model. **A** H&E-stained images of cross-sectioned wound tissues from all five groups at days 6 and 9 post-implantation. Blue dotted lines indicate wound boundaries. **B** Picrosirius red (PSR)-stained images showing collagen fiber deposition at day 6. **C** Immunohistochemical staining of CD31 and α-SMA in cross-sectioned skin tissues at the wound periphery on day 6. **D**–**F** Quantification of CD31-positive capillaries, α-SMA-positive arterioles, and vessel size was performed using $n=3$ biological replicates (independent animals), with multiple images analyzed per sample. NS, not significant. $*p<0.05$, $*p<0.01$, $*p<0.001$, $*p<0.0001$

MSC spheroid–embedded prevascularized grafts enhance therapeutic angiogenesis in a critical limb ischemia model

To assess the therapeutic efficacy of the prevascularized graft developed in this study, an in vivo experiment was conducted using a mouse model of critical limb ischemia. The model was generated by surgically excising a portion of the femoral arteriovenous bundle (Fig. 7A). Three types of constructs—μVP Only, Spheroid Only, and μVP + spheroid—were fabricated and implanted at the ischemic site. Each construct ($6 \times 8 \times 1$ mm^3) was designed to contain 18 MSC spheroids, reflecting the implantable dimensions suitable for the mouse limb. This spheroid number was also selected in reference to the previously identified optimal range (16–24). To assess the host regenerative response and baseline effect of the acellular hydrogel, no-treatment and hydrogel-only groups (No Treat and Gel Only) were included as controls. Ischemic progression of the operated limb was monitored after surgical procedure(Fig. 7B). To determine an appropriate evaluation time point, a pilot study was conducted to compare outcomes at 2 and 4 weeks post-implantation (Fig. S9). No substantial differences in limb outcomes were observed. Therefore, 2 weeks timepoint was selected as the primary endpoint, consistent with previous studies evaluating early therapeutic responses [69–71]. By day 3, severe tissue necrosis was observed in the control group. By day 14, limb loss occurred in 78.57% of the untreated mice and 63.63% of those receiving hydrogel alone (Fig. 7C). Constructs containing a single component (μVP Only and spheroid Only) exhibited slightly reduced necrosis than controls, but above 50% of the animals still experienced limb loss by day 14. Contrarily, the μVP + spheroid group demonstrated considerably improved outcomes, with 64.29% limb preservation and only 14.28% limb loss, highlighting its superior therapeutic effects. While the hindlimb ischemia model is well-established, therapeutic outcomes can vary substantially depending on surgical procedures and experimental conditions [30]. Nevertheless, previously reported limb salvage rates under comparable conditions generally fall within a similar range [35, 37, 70–72], indicating that our results are consistent with prior studies.

Two weeks after implantation, muscle tissues from the ischemic limb at the implantation site were harvested for histological analysis. H&E and Masson's trichrome staining revealed severe muscle degeneration and fibrosis in the untreated and Gel Only groups, respectively (Fig. 7D). The μVP- and Spheroid Only groups exhibited moderate tissue damage, while the μVP + spheroid group exhibited well-preserved, densely aligned muscle fibers. To evaluate microvascular preservation, immunohistochemical staining using anti-CD31 and anti-α-SMA antibodies was performed (Fig. 8A). Quantitative analyses demonstrated that the μVP + spheroid group possessed considerably higher capillary density and arteriole counts than all other groups (Fig. 8B and C). Furthermore, diameter analysis of α-SMA–positive arterioles indicated that the μVP + spheroid group had numerous arterioles and a larger average vessel diameter (Fig. 8D).

To evaluate the in vivo functionality of μVPs within the prevascularized graft, constructs from the μVP + spheroid group were explanted on day 3 and subjected to co-immunostained for engineered vessels (GFP-positive ECs) and host vessels (mouse CD31) (Fig. 8E). Overlapping signals for both markers were observed within the μVP regions, indicating vascular integration and the formation of chimeric vessels composed of host and engineered capillaries within implanted grafts. Z-stacked confocal imaging revealed that host vessels surrounded the implanted

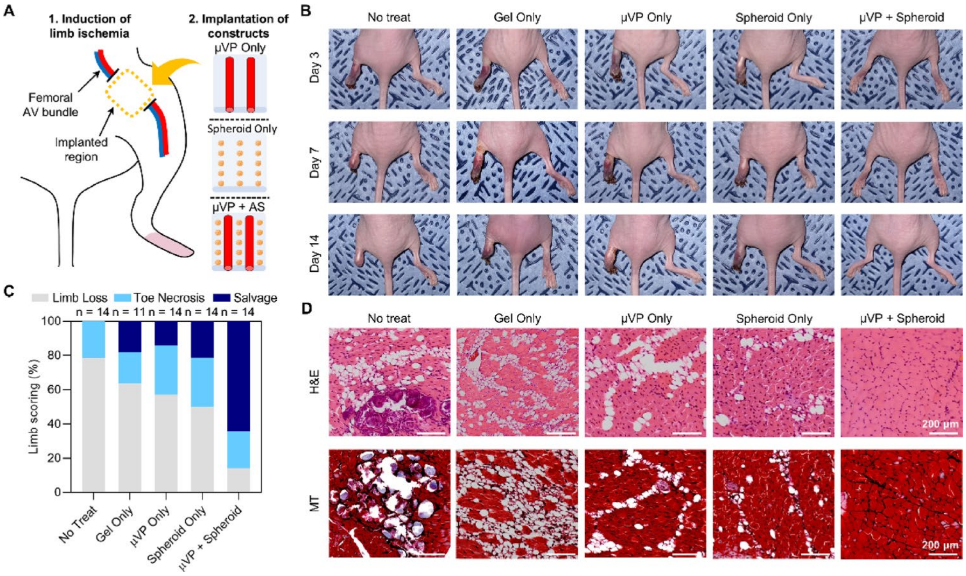

Fig. 7 *In vivo* therapeutic effects of bioprinted grafts in a murine critical limb ischemia model. **A** Schematic illustration showing the experimental design to investigate the in vivo regenerative effects of prevascularized grafts on a critical limb ischemia mouse model. **B** Representative photographs of mice showing serial changes in ischemic limbs on days 3, 7, and 14. **C** Scoring graph for the physiological status of ischemic limbs on day 14 ($n = 11$–14). **D** H&E (upper) and Masson's trichrome (MT) (lower) staining results of cross-sectioned ischemic muscle from the quadriceps at the implantation site 14 days post-implantation

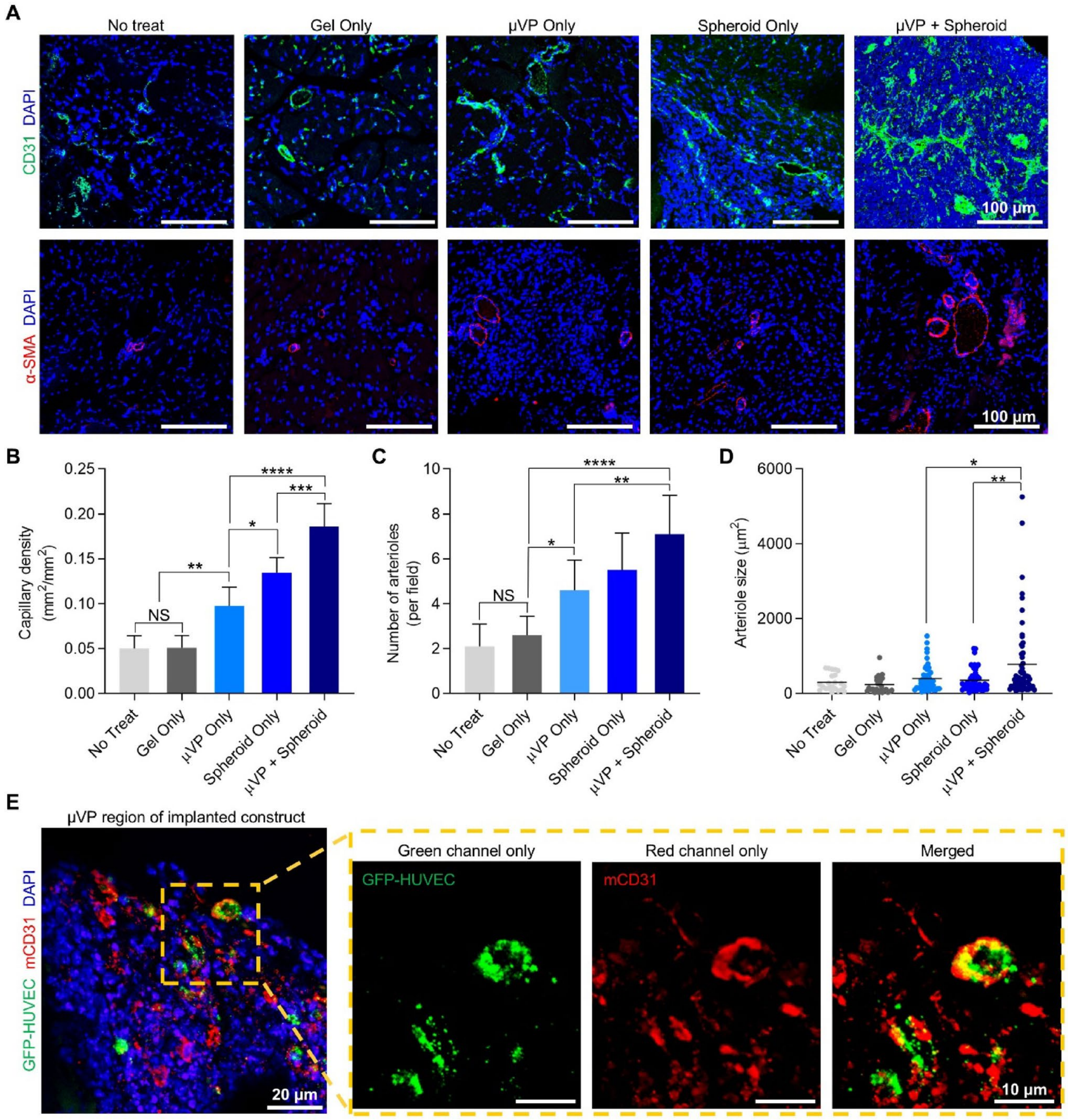

Fig. 8 Histological evaluation of bioprinted and implanted grafts on ischemic disease model. **A** Immunohistochemical images with CD31 and α-SMA in cross-sectioned ischemic muscles. **B**–**D** Quantification of CD31-positive capillary density, α-SMA-positive arterioles, and arteriole size was performed using $n = 3$ biological replicates (independent animals), with multiple images analyzed per sample. $^{*}p < 0.05$, $^{**}p < 0.01$, $^{***}p < 0.001$, and $^{****}p < 0.0001$. **E** Immunohistochemical images with anti-GFP antibody (implanted endothelial cells, green) and anti-mCD31 antibody (host endothelial cells, red) within μVP regions of cross-sectioned grafts 3 days post-implantation

vasculature, with host-derived signals decreasing at greater depths along the z-axis, while engineered vessels with larger lumens became more prominent (Fig. S10). These results correspond with previous studies showing that the host vasculature integrates with implanted vascular structures through perivascular interactions and anastomosis formation [38, 39, 73]. Such integration enhances therapeutic angiogenesis, as reported in previous studies [34–36]. Overall, our findings indicate that prevascularized graft—incorporating μVPs capable of vascular integration with highly angiogenic MSC spheroids—achieves enhanced therapeutic efficacy in ischemic tissue environments.

Numerous biomolecules, biomaterials, and cell-based approaches have been investigated for ischemic therapy [74]. Among these, MSCs have demonstrated enhanced secretion of angiogenic factors and superior in vivo regenerative effects [17–21], and are currently under clinical investigation for myocardial infarction and critical limb ischemia [22–24]. Hydrogel-based implants have emerged as effective delivery platforms [30–32], with prevascularized hydrogel exhibiting promise in restoring perfusion by promoting neovascularization and enhancing therapeutic angiogenesis in ischemic tissues [33–37]. Preformed vascular structures have been demonstrated to promote neovascularization and integrate with the host vasculature [34, 35]. Further, spatially organized vasculature promotes host integration with implanted constructs and improves therapeutic outcomes in ischemic models [34–36]. However, numerous prevascularized constructs comprise only ECs and lack sufficient angiogenic factor secretion, thereby limiting their ability to initiate early host neovascularization and reducing their therapeutic efficacy in ischemia. Successful integration of engineered grafts with host vasculature critically relies on host vessel infiltration via neovascularization, a crucial step for forming functionally connected microvessels [38].

To address this limitation, we developed a printing technique that enables precise spatial controlling of prevascularized patterns and positioning of angiogenic spheroids, thereby enhancing anastomosis with host vessels and regenerative efficacy in ischemic tissues. Based on our previous study [44], the printed MSCs formed spheroid-like structures, maintained their stem-like phenotypes, and exhibited high VEGF secretion under optimized matrix conditions (Fig. 2). Using this approach, MSC spheroids could be positioned at defined distances from the μVPs (Fig. 3), with spheroids approximately 250 μm away promoting enhanced EC-MSCs crosstalk, capillary formation, and maturation. Following implantation into dorsal subcutaneous tissue, which has low vascular density [66], the incorporation of MSC spheroids significantly enhanced neovascularization, and EC-derived vessel structures within the μVP regions were retained after transplantation (Fig. 4). In addition, variation in neovascularization across spheroid configurations near the μVP suggests that spatial organization of angiogenic factor sources is important for functional graft vascularization, consistent with our previous findings [40]. Notably, prevascularized constructs containing MSC spheroids showed accelerated wound closure and improved perfusion recovery (Fig. 5). Furthermore, μVP+spheroid constructs demonstrated superior therapeutic efficacy in a critical limb ischemia model than constructs containing only either μVP or spheroids (Fig. 7). However, these effects may have been attributable to an increased total cell number within the μVP+spheroid constructs. To investigate the interactive effects of both components, comparative experiments were conducted using constructs containing either 12 or 24 spheroids alone versus μVP+12 spheroids (Fig. S11A). The 24-spheroid-only construct, despite having twice the MSC spheroid number, resulted in a lower limb salvage rate than the μVP+12 spheroids group, which achieved ~50% limb salvage with only half the spheroid number (Fig. S11B). Conversely, the μVP+24 spheroids group exhibited even higher limb loss rates despite the increased spheroid count. These results correspond with the subcutaneous implantation findings, wherein excessive spheroid density led to reduced neovascularization, likely due to hypoxic conditions within the implant (Fig. 4). This is also consistent with our previous findings, where excessive spheroid densities resulted in poor graft vascularization and reduced implanted cell viability, as confirmed by TUNEL staining after the transplantation [42]. These findings demonstrate the synergistic therapeutic effect of combining μVPs with MSC spheroids, while highlighting the importance of spatially designed spheroid distribution to avoid adverse therapeutic outcomes associated with overly dense cell populations.

In this study, we developed a dual-function prevascularized graft fabrication strategy using in-bath bioprinting, enabling precise spatial positioning of highly angiogenic MSC spheroids alongside the formation of densely patterned capillaries. This approach offers a notable technical advancement over conventional spheroid fabrication and prevascularized hydrogel methods, which lack the spatial resolution necessary for maintaining pattern fidelity. Further, the platform allowed quantitative assessment of paracrine interactions as a function of the distance between μVPs and MSC spheroids (Fig. 3). The platform also provides a versatile framework for investigating interactions between microvascular structures and biological models such as cancer aggregates or organoids. As the constructs are fabricated within a 3D hydrogel matrix, the technique is readily scalable, providing translational potential for clinically relevant grafts while maintaining optimized parameters. Our findings indicate that incorporating 18 MSC spheroids within a 6 × 8 × 1 mm³ graft resulted in the most effective therapeutic outcome in ischemic rescue (Figs. 7 and 8), suggesting the potential for broader application, although further validation in clinically relevant models is needed. While the mouse hindlimb ischemia model is widely used for proof-of-concept studies for ischemia therapy [43], it does not fully recapitulate the complexity of human clinical conditions, particularly in terms of scale. To explore the translational potential of this strategy toward clinically relevant scales, we next fabricated larger-area constructs applicable to ischemic diseases such as myocardial infarction, where several preclinical studies for the treatment of mild myocardial infarction have reported graft sizes on the order of ~10 cm^2 [75, 76]. Based on this consideration, a cell-free hydrogel construct with dimensions of approximately 3.2 × 3.2 × 0.1 cm^3 was fabricated (Fig. S12). Within this construct, 224 MSC spheroids and 13 parallel µVPs were spatially organized while maintaining sufficient mechanical integrity for graft handling, demonstrating the feasibility of scaling up the proposed fabrication strategy to human-scale constructs while preserving architectural control of vascular and spheroid components. However, this study was conducted using an immunodeficient animal model, which does not fully capture the role of immune responses that are critical for vascular regeneration. For large-scale constructs and clinical applications, additional supporting strategies such as oxygen-generating hydrogels and immune-modulating biomaterials may be required to enhance cell viability under hypoxic conditions and modulate host immune responses through macrophage polarization [77, 78]. In addition, while HUVECs were used in this study for their accessibility and reproducibility, autologous endothelial cells such as induced pluripotent stem cell (iPSC)-derived ECs could be incorporated in future clinical applications to improve translational relevance and reduce immunological concerns [79]. Additionally, given that the geometric configuration of microvascular structures considerably affects blood flow recovery in ischemic tissues [34–36], future studies will investigate engineering human-scale µVP architectures to promote rapid neovascularization and collateral circulation formation. In addition to ischemic repair, this strategy may be applicable to other grafts requiring prevascularization, such as islet transplantation in subcutaneous implantation sites, which are surgically accessible yet poorly vascularized [39, 80]. Precisely controlling the spatial arrangement of MSC spheroids and µVPs to enhance vascularization while maintaining distinct islet-encapsulating regions may provide a promising approach for constructing durable, large-scale grafts. We believe that optimizing the synergistic functions of µVPs and spheroids will establish a foundation for translationally relevant graft designs capable of enhanced angiogenic performance and therapeutic effect into ischemic tissues.

Conclusion

We developed a dual-function prevascularized graft that leverages the synergistic effects of spatially organized MSC spheroids and µVPs to enhance therapeutic angiogenesis in ischemic tissues. By optimizing fabrication parameters, highly angiogenic MSC spheroids and pre-matured capillary bundles were successfully incorporated into the printed grafts. Grafts containing an optimal number of MSC spheroids promoted robust host vessel infiltration into µVP regions, supported the retention of implanted-EC derived vascular structures, and achieved superior therapeutic outcomes in ischemic tissue models. Together, these findings establish a novel therapeutic strategy for enhancing angiogenesis and restoring blood perfusion, and may provide a basis for future translational applications in ischemic disease treatment.

Supplementary Information The online version contains supplementary material available at https://doi.org/10.1007/s10456-026-10059-3.

Acknowledgements This research was supported by the Nano & Material Technology Development Program through the National Research Foundation of Korea (NRF) funded by Ministry of Science and ICT (RS-2024-00407234) and the Bio&Medical Technology Development Program of the National Research Foundation (NRF) funded by the Korean government (MSIT) (No. RS-2024-00508821). The authors thank the UNIST Central Research Facilities (UCRF), particularly the In Vivo Research Center (IVRC), for access to essential equipment and technical support. We also gratefully acknowledge Dr. Sooah Park and Mr. Hong-Chan Joung for her continued technical assistance.

Author contributions J.S., A.N., H.J.M. contributed equally to this work and should be considered as co-first authors. J.S.: Conceptualization, Formal analysis, Investigation, Methodology, Visualization, Writing – original draft, Writing – review & editing. A.N.: Formal analysis, Investigation, Methodology, Visualization, Writing – original draft. H.J.M.: Investigation, Formal analysis, Methodology, Visualization. M.A.: Investigation, Methodology, Visualization. W.H.: Methodology, Investigation. M.K.K.: Investigation, Methodology. S.J.: Methodology, Validation. B.S.K.: Methodology, Validation. Y.K.C.: Methodology, Writing – review & editing. S.T.: Methodology, Writing – review & editing. H.W.K.: Conceptualization, Project administration, Funding acquisition, Supervision, Writing – original draft. Writing – review & editing.

Funding Open Access funding enabled and organized by Ulsan National Institute of Science and Technology (UNIST)

Data availability Data is provided within the manuscript and is available for review upon request.

Declarations

Conflict of interest The authors declare no competing interests.

Ethics approval All animal studies were conducted with approval from the Institutional Animal Care and Use Committee (IACUC) at UNIST (protocol number - UNIST-IACUC-23-39) and Pusan National University (PNU-2026-0751). The authors declare that all experiments involving animals follow all relevant ethical regulations.

References

1. Eltzschig HK, Eckle T (2011) Ischemia and reperfusion: from mechanism to translation. Nat Med 17(11):1391–1401. https://doi.org/10.1038/nm.2507
2. Kalogeris T, Baines CP, Krenz M, Korthuis RJ (2017) Ischemia/reperfusion. Compr Physiol 7(1):113–170. https://doi.org/10.1002/j.2040-4603.2017.tb00741.x
3. Heusch G (2024) Myocardial ischemia/reperfusion: translational pathophysiology of ischemic heart disease. Med (N Y) 5(1):10–31. https://doi.org/10.1016/j.medj.2023.12.007
4. Virani SS, Alonso A, Aparicio HJ, Benjamin EJ, Bittencourt MS, Callaway CW, Carson AP, Chamberlain AM, Cheng S, Delling FN, Elkind MSV, Evenson KR, Ferguson JF, Gupta DK, Khan SS, Kissela BM, Knutson KL, Lee CD, Lewis TT, Liu J, Loop MS, Lutsey PL, Ma J, Mackey J, Martin SS, Matchar DB, Mussolino ME, Navaneethan SD, Perak AM, Roth GA, Samad Z, Satou GM, Schroeder EB, Shah SH, Shay CM, Stokes A, VanWagner LB, Wang N-Y, Tsao CW, Epidemiology OAHAC, Committee PS, Subcommittee SS (2021) Heart disease and stroke statistics—2021 update. Circulation 143(8):e254–e743. https://doi.org/10.1161/CIR.0000000000000950
5. Tam DY, Dharma C, Rocha R, Farkouh ME, Abdel-Qadir H, Sun LY, Wijeysundera HC, Austin PC, Udell JA, Gaudino M, Fremes SE, Lee DS (2020) Long-term survival after surgical or percutaneous revascularization in patients with diabetes and multivessel coronary disease. J Am Coll Cardiol 76(10):1153–1164. https://doi.org/10.1016/j.jacc.2020.06.052
6. Slovut DP, Lipsitz EC (2012) Surgical technique and peripheral artery disease. Circulation 126(9):1127–1138. https://doi.org/10.1161/CIRCULATIONAHA.111.059048
7. Berry C, Tardif J-C, Bourassa Martial G (2007) Coronary heart disease in patients with diabetes. J Am Coll Cardiol 49(6):643–656. https://doi.org/10.1016/j.jacc.2006.09.045
8. Beckman JA, Schneider PA, Conte MS (2021) Advances in revascularization for peripheral artery disease: revascularization in PAD. Circ Res 128(12):1885–1912. https://doi.org/10.1161/CIRCRESAHA.121.318261
9. Kappetein AP, van Mieghem NM, Head SJ (2014) Revascularization options: coronary artery bypass surgery and percutaneous coronary intervention. Cardiol Clin 32(3):457–461. https://doi.org/10.1016/j.ccl.2014.04.011
10. Jukema JW, Ahmed TAN, Verschuren JJW, Quax PHA (2012) Restenosis after PCI. Part 2: prevention and therapy. Nat Rev Cardiol 9(2):79–90. https://doi.org/10.1038/nrcardio.2011.148
11. Dangas GD, Claessen BE, Caixeta A, Sanidas EA, Mintz GS, Mehran R (2010) In-stent restenosis in the drug-eluting stent era. J Am Coll Cardiol 56(23):1897–1907. https://doi.org/10.1016/j.jacc.2010.07.028
12. Fantini DA, Yang G, Khanna A, Subramanian D, Phillippi JA, Huang NF (2024) Overcoming big bottlenecks in vascular regeneration. Commun Biol 7(1):876. https://doi.org/10.1038/s42003-024-06567-x
13. Baccouche BM, Elde S, Wang H, Woo YJ (2024) Structural, angiogenic, and immune responses influencing myocardial regeneration: a glimpse into the crucible. npj Regen Med 9(1):18. https://doi.org/10.1038/s41536-024-00357-z
14. Simons M, Ware JA (2003) Therapeutic angiogenesis in cardiovascular disease. Nat Rev Drug Discov 2(11):863–872. https://doi.org/10.1038/nrd1226
15. Annex BH (2013) Therapeutic angiogenesis for critical limb ischaemia. Nat Rev Cardiol 10(7):387–396. https://doi.org/10.1038/nrcardio.2013.70
16. Chen X, Yu W, Zhang J, Fan X, Liu X, Liu Q, Pan S, Dixon RAF, Li P, Yu P, Shi A (2023) Therapeutic angiogenesis and tissue revascularization in ischemic vascular disease. J Biol Eng 17(1):13. https://doi.org/10.1186/s13036-023-00330-2
17. Henry TD, Annex BH, McKendall GR, Azrin MA, Lopez JJ, Giordano FJ, Shah PK, Willerson JT, Benza RL, Berman DS, Gibson CM, Bajamonde A, Rundle AC, Fine J, McCluskey ER (2003) The VIVA trial. Circulation 107(10):1359–1365. https://doi.org/10.1161/01.CIR.0000061911.47710.8A
18. Beheshtizadeh N, Gharibshahian M, Bayati M, Maleki R, Strachan H, Doughty S, Tayebi L (2023) Vascular endothelial growth factor (VEGF) delivery approaches in regenerative medicine. Biomed Pharmacother 166:115301. https://doi.org/10.1016/j.biopha.2023.115301
19. Dimmeler S, Burchfield J, Zeiher AM (2008) Cell-based therapy of myocardial infarction. Arterioscler Thromb Vasc Biol 28(2):208–216. https://doi.org/10.1161/ATVBAHA.107.155317
20. Golpanian S, Wolf A, Hatzistergos KE, Hare JM (2016) Rebuilding the damaged heart: mesenchymal stem cells, cell-based therapy, and engineered heart tissue. Physiol Rev 96(3):1127–1168. https://doi.org/10.1152/physrev.00019.2015
21. Johnson T, Zhao L, Manuel G, Taylor H, Liu D (2019) Approaches to therapeutic angiogenesis for ischemic heart disease. J Mol Med 97(2):141–151. https://doi.org/10.1007/s00109-018-1729-3
22. Morishita R, Makino H, Aoki M, Hashiya N, Yamasaki K, Azuma J, Taniyama Y, Sawa Y, Kaneda Y, Ogihara T (2011) Phase I/IIa clinical trial of therapeutic angiogenesis using hepatocyte growth factor gene transfer to treat critical limb ischemia. Arterioscler Thromb Vasc Biol 31(3):713–720. https://doi.org/10.1161/ATVBAHA.110.219550
23. Perin EC, Silva GV (2011) Cell-based therapy for chronic ischemic heart disease: a clinical perspective. Cardiovasc Ther 29(3):211–217. https://doi.org/10.1111/j.1755-5922.2010.00214.x
24. Shirbaghaee Z, Hassani M, Heidari Keshel S, Soleimani M (2022) Emerging roles of mesenchymal stem cell therapy in patients with critical limb ischemia. Stem Cell Res Ther 13(1):462. https://doi.org/10.1186/s13287-022-03148-9
25. Sterodimas A, de Faria J, Nicaretta B, Pitanguy I (2010) Tissue engineering with adipose-derived stem cells (ADSCs): current and future applications. J Plast Reconstr Aesthet Surg 63(11):1886–1892. https://doi.org/10.1016/j.bjps.2009.10.028
26. Kouroupis D, Correa D (2021) Increased mesenchymal stem cell functionalization in three-dimensional manufacturing settings for enhanced therapeutic applications. Front Bioeng Biotechnol 9:621748. https://doi.org/10.3389/fbioe.2021.621748
27. Petrenko Y, Syková E, Kubinová Š (2017) The therapeutic potential of three-dimensional multipotent mesenchymal stromal cell spheroids. Stem Cell Res Ther 8(1):94. https://doi.org/10.1186/s13287-017-0558-6
28. Sart S, Tsai A-C, Li Y, Ma T (2014) Three-dimensional aggregates of mesenchymal stem cells: cellular mechanisms, biological properties, and applications. Tissue Eng Part B Rev 20(5):365–380. https://doi.org/10.1089/ten.teb.2013.0537
29. Van Hove AH, Benoit DS (2015) Depot-based delivery systems for pro-angiogenic peptides: a review. Front Bioeng Biotechnol 3:102. https://doi.org/10.3389/fbioe.2015.00102

30. Xing Z, Zhao C, Wu S, Zhang C, Liu H, Fan Y (2021) Hydrogel-based therapeutic angiogenesis: an alternative treatment strategy for critical limb ischemia. Biomaterials 274:120872. https://doi.org/10.1016/j.biomaterials.2021.120872
31. Costa ALR, Willerth SM, de la Torre LG, Han SW (2022) Trends in hydrogel-based encapsulation technologies for advanced cell therapies applied to limb ischemia. Mater Today Bio 13:100221. https://doi.org/10.1016/j.mtbio.2022.100221
32. Rotaru-Zăvăleanu A-D, Dinescu VC, Aldea M, Gresita A (2024) Hydrogel-based therapies for ischemic and hemorrhagic stroke: a comprehensive review. Gels 10(7):476. https://doi.org/10.3390/gels10070476
33. Riemenschneider SB, Mattia DJ, Wendel JS, Schaefer JA, Ye L, Guzman PA, Tranquillo RT (2016) Inosculation and perfusion of pre-vascularized tissue patches containing aligned human microvessels after myocardial infarction. Biomaterials 97:51–61. https://doi.org/10.1016/j.biomaterials.2016.04.031
34. Mirabella T, MacArthur JW, Cheng D, Ozaki CK, Woo YJ, Yang MT, Chen CS (2017) 3D-printed vascular networks direct therapeutic angiogenesis in ischaemia. Nat Biomed Eng 1(6):0083. https://doi.org/10.1038/s41551-017-0083
35. Kang B, Shin J, Park H-J, Rhyou C, Kang D, Lee S-J, Yoon Y-s, Cho S-W, Lee H (2018) High-resolution acoustophoretic 3D cell patterning to construct functional collateral cylindroids for ischemia therapy. Nat Commun 9(1):5402. https://doi.org/10.1038/s41467-018-07823-5
36. Redd MA, Zeinstra N, Qin W, Wei W, Martinson A, Wang Y, Wang RK, Murry CE, Zheng Y (2019) Patterned human microvascular grafts enable rapid vascularization and increase perfusion in infarcted rat hearts. Nat Commun 10(1):584. https://doi.org/10.1038/s41467-019-08388-7
37. Bang S, Tahk D, Choi YH, Lee S, Lim J, Lee S-R, Kim B-S, Kim HN, Hwang NS, Jeon NL (2022) 3D Microphysiological system-inspired scalable vascularized tissue constructs for regenerative medicine. Adv Funct Mater 32(1):2105475. https://doi.org/10.1002/adfm.202105475
38. Cheng G, Liao S, Kit Wong H, Lacorre DA, Di Tomaso E, Au P, Fukumura D, Jain RK, Munn LL (2011) Engineered blood vessel networks connect to host vasculature via wrapping-and-tapping anastomosis. Blood 118(17):4740–4749. https://doi.org/10.1182/blood-2011-02-338426
39. Song W, Chiu A, Wang L-H, Schwartz RE, Li B, Bouklas N, Bowers DT, An D, Cheong SH, Flanders JA, Pardo Y, Liu Q, Wang X, Lee VK, Dai G, Ma M (2019) Engineering transferrable microvascular meshes for subcutaneous islet transplantation. Nat Commun 10(1):4602. https://doi.org/10.1038/s41467-019-12373-5
40. Son J, Mohamed HJ, Ha W, Naren A, Choi C, Kwon YH, Park S, Joung H-C, Kang H-W (2023) Bioprinting of pre-vascularized constructs for enhanced in vivo neo-vascularization. Biofabrication 15(3):034101. https://doi.org/10.1088/1758-5090/acc9de
41. Ben-Shaul S, Landau S, Merdler U, Levenberg S (2019) Mature vessel networks in engineered tissue promote graft–host anastomosis and prevent graft thrombosis. Proc Natl Acad Sci USA 116(8):2955–2960. https://doi.org/10.1073/pnas.1814238116
42. Mohamed HJ, Jeong W, Son J, Kang HW (2025) Bioprinting of adipose tissue graft with enhanced neo-vessel formation in vivo. Adv Healthc Mater 2500627. https://doi.org/10.1002/adhm.202500627
43. Limbourg A, Korff T, Napp LC, Schaper W, Drexler H, Limbourg FP (2009) Evaluation of postnatal arteriogenesis and angiogenesis in a mouse model of hind-limb ischemia. Nat Protoc 4(12):1737–1748. https://doi.org/10.1038/nprot.2009.185
44. Jeon S, Heo J-H, Kim MK, Jeong W, Kang H-W (2020) High-precision 3D bio-dot printing to improve paracrine interaction between multiple types of cell spheroids. Adv Funct Mater 30(52):2005324. https://doi.org/10.1002/adfm.202005324
45. Shikanov A, Xu M, Woodruff TK, Shea LD (2009) Interpenetrating fibrin–alginate matrices for in vitro ovarian follicle development. Biomaterials 30(29):5476–5485. https://doi.org/10.1016/j.biomaterials.2009.06.054
46. Vorwald CE, Gonzalez-Fernandez T, Joshee S, Sikorski P, Leach JK (2020) Tunable fibrin-alginate interpenetrating network hydrogels to support cell spreading and network formation. Acta Biomater 108:142–152. https://doi.org/10.1016/j.actbio.2020.03.014
47. Zhou Y, Yue Z, Chen Z, Wallace G (2020) 3D coaxial printing tough and elastic hydrogels for tissue engineering using a catechol functionalized ink system. Adv Healthc Mater 9(24):2001342. https://doi.org/10.1002/adhm.202001342
48. Volpi M, Paradiso A, Costantini M, Święszkowski W (2022) Hydrogel-based fiber biofabrication techniques for skeletal muscle tissue engineering. Acs Biomater Sci Eng 8(2):379–405. https://doi.org/10.1021/acsbiomaterials.1c01145
49. Kozan NG, Joshi M, Sicherer ST, Grasman JM (2023) Porous biomaterial scaffolds for skeletal muscle tissue engineering. Front Bioeng Biotechnol Volume 11–2023. https://doi.org/10.3389/fbioe.2023.1245897
50. Freeman FE, Kelly DJ (2017) Tuning alginate bioink stiffness and composition for controlled growth factor delivery and to spatially direct MSC fate within bioprinted tissues. Sci Rep 7(1):17042. https://doi.org/10.1038/s41598-017-17286-1
51. de Melo BA, Jodat YA, Mehrotra S, Calabrese MA, Kamperman T, Mandal BB, Santana MH, Alsberg E, Leijten J, Shin SR (2019) 3D printed cartilage-like tissue constructs with spatially controlled mechanical properties. Adv Funct Mater 29(51):1906330. https://doi.org/10.1002/adfm.201906330
52. Liu Z, Zhao B, Zhang L, Qian S, Mao J, Cheng L, Mao X, Cai Z, Zhang Y, Cui W, Sun X (2022) Modulated integrin signaling receptors of stem cells via ultra-soft hydrogel for promoting angiogenesis. Compos Part B: Eng 234:109747. https://doi.org/10.1016/j.compositesb.2022.109747
53. Kim EM, Lee GM, Lee S, Kim S-j, Lee D, Yoon DS, Joo J, Kong H, Park HH, Shin H (2022) Effects of mechanical properties of gelatin methacryloyl hydrogels on encapsulated stem cell spheroids for 3D tissue engineering. Int J Biol Macromol 194:903–913. https://doi.org/10.1016/j.ijbiomac.2021.11.145
54. Im G-B, Kim S-W, Bhang SH (2021) Fortifying the angiogenic efficacy of adipose derived stem cell spheroids using spheroid compaction. J Ind Eng Chem 93:228–236. https://doi.org/10.1016/j.jiec.2020.09.027
55. Lee J, Lee S, Kim SM, Shin H (2021) Size-controlled human adipose-derived stem cell spheroids hybridized with single-segmented nanofibers and their effect on viability and stem cell differentiation. Biomater Res 25(1):14. https://doi.org/10.1186/s40824-021-00215-9
56. Bhang SH, Cho S-W, La W-G, Lee T-J, Yang HS, Sun A-Y, Baek S-H, Rhie J-W, Kim B-S (2011) Angiogenesis in ischemic tissue produced by spheroid grafting of human adipose-derived stromal cells. Biomaterials 32(11):2734–2747. https://doi.org/10.1016/j.biomaterials.2010.12.035
57. Cui L, Luo Y, Wang H, Chen Q, Zhou X, Guan Y, Zhang Y (2022) Uniformly sized stem cell spheroids for treatment of hind limb ischemia: size effect. Adv Mater Interfaces 9(14):2102327. https://doi.org/10.1002/admi.202102327
58. Rovere M, Reverberi D, Arnaldi P, Palamà MEF, Gentili C (2023) Spheroid size influences cellular senescence and angiogenic potential of mesenchymal stromal cell-derived soluble factors and extracellular vesicles. Front Bioeng Biotechnol 11:1297644
59. Freiman A, Shandalov Y, Rosenfeld D, Shor E, Ben-David D, Meretzki S, Levenberg S, Egozi D (2018) Engineering vascularized flaps using adipose-derived microvascular endothelial cells and mesenchymal stem cells. J Tissue Eng Regen Med 12(1):e130–e141. https://doi.org/10.1002/term.2436

60. Barrs RW, Jia J, Ward M, Richards DJ, Yao H, Yost MJ, Mei Y (2020) Engineering a chemically defined hydrogel bioink for direct bioprinting of microvasculature. Biomacromolecules 22(2):275–288. https://doi.org/10.1021/acs.biomac.0c00947
61. Piard C, Jeyaram A, Liu Y, Caccamese J, Jay SM, Chen Y, Fisher J (2019) 3D printed HUVECs/MSCs cocultures impact cellular interactions and angiogenesis depending on cell-cell distance. Biomaterials 222:119423. https://doi.org/10.1016/j.biomaterials.2019.119423
62. Friend NE, Beamish JA, Margolis EA, Schott NG, Stegemann JP, Putnam AJ (2024) Pre-cultured, cell-encapsulating fibrin microbeads for the vascularization of ischemic tissues. J Biomedical Mater Res Part A 112(4):549–561. https://doi.org/10.1002/jbm.a.37580
63. Wang L-H, Ernst AU, Flanders JA, Liu W, Wang X, Datta AK, Epel B, Kotecha M, Papas KK, Ma M (2021) An inverse-breathing encapsulation system for cell delivery. Sci Adv 7(20):eabd5835. https://doi.org/10.1126/sciadv.abd5835
64. Wang L-H, Marfil-Garza BA, Ernst AU, Pawlick RL, Pepper AR, Okada K, Epel B, Viswakarma N, Kotecha M, Flanders JA, Datta AK, Gao H-J, You Y-Z, Ma M, Shapiro AMJ (2024) Inflammation-induced subcutaneous neovascularization for the long-term survival of encapsulated islets without immunosuppression. Nat Biomed Eng 8(10):1266–1284. https://doi.org/10.1038/s41551-023-01145-8
65. Shukla AK, Ahn M, Gao J, Lee D, Yoon S, Oh S-O, Gao G, Cho W-W, Kim BS (2026) Exploring the angiogenic potential of skin patches with endothelial cell patterns fabricated via in-bath 3D bioprinting using light-activated bioink for enhanced wound healing. Biomaterials 325:123575. https://doi.org/10.1016/j.biomaterials.2025.123575
66. Nowak-Sliwinska P, Alitalo K, Allen E, Anisimov A, Aplin AC, Auerbach R, Augustin HG, Bates DO, van Beijnum JR, Bender RHF, Bergers G, Bikfalvi A, Bischoff J, Böck BC, Brooks PC, Bussolino F, Cakir B, Carmeliet P, Castranova D, Cimpean AM, Cleaver O, Coukos G, Davis GE, De Palma M, Dimberg A, Dings RPM, Djonov V, Dudley AC, Dufton NP, Fendt S-M, Ferrara N, Fruttiger M, Fukumura D, Ghesquière B, Gong Y, Griffin RJ, Harris AL, Hughes CCW, Hultgren NW, Iruela-Arispe ML, Irving M, Jain RK, Kalluri R, Kalucka J, Kerbel RS, Kitajewski J, Klaassen I, Kleinmann HK, Koolwijk P, Kuczynski E, Kwak BR, Marien K, Melero-Martin JM, Munn LL, Nicosia RF, Noel A, Nurro J, Olsson A-K, Petrova TV, Pietras K, Pili R, Pollard JW, Post MJ, Quax PHA, Rabinovich GA, Raica M, Randi AM, Ribatti D, Ruegg C, Schlingemann RO, Schulte-Merker S, Smith LEH, Song JW, Stacker SA, Stalin J, Stratman AN, Van de Hinsbergh VM, Vermeulen VWM, Waltenberger PB, Weinstein J, Xin BM, Yetkin-Arik H, Yla-Herttuala B, Yoder S, Griffioen MC AW (2018) Consensus guidelines for the use and interpretation of angiogenesis assays. Angiogenesis 21(3):425–532. https://doi.org/10.1007/s10456-018-9613-x
67. Peña OA, Martin P (2024) Cellular and molecular mechanisms of skin wound healing. Nat Rev Mol Cell Biol 25(8):599–616. https://doi.org/10.1038/s41580-024-00715-1
68. Xue M, Jackson CJ (2015) Extracellular matrix reorganization during wound healing and its impact on abnormal scarring. Adv Wound Care 4(3):119–136. https://doi.org/10.1089/wound.2013.0485
69. Lee S, Valmikinathan CM, Byun J, Kim S, Lee G, Mokarram N, Pai SB, Um E, Bellamkonda RV, Yoon Y-s (2015) Enhanced therapeutic neovascularization by CD31-expressing cells and embryonic stem cell-derived endothelial cells engineered with chitosan hydrogel containing VEGF-releasing microtubes. Biomaterials 63:158–167. https://doi.org/10.1016/j.biomaterials.2015.06.009
70. Kim SJ, Jun I, Kim DW, Lee YB, Lee YJ, Lee J-H, Park KD, Park H, Shin H (2013) Rapid Transfer of endothelial cell sheet using a thermosensitive hydrogel and its effect on therapeutic angiogenesis. Biomacromolecules 14(12):4309–4319. https://doi.org/10.1021/bm4011744
71. Lee JB, Kim D-H, Yoon J-K, Park DB, Kim H-S, Shin YM, Baek W, Kang M-L, Kim HJ, Sung H-J (2020) Microchannel network hydrogel induced ischemic blood perfusion connection. Nat Commun 11(1):615. https://doi.org/10.1038/s41467-020-14480-0
72. Jun I, Ahmad T, Bak S, Lee J-Y, Kim EM, Lee J, Lee YB, Jeong H, Jeon H, Shin H (2017) Spatially assembled bilayer cell sheets of stem cells and endothelial cells using thermosensitive hydrogels for therapeutic angiogenesis. Adv Healthc Mater 6(9):1601340. https://doi.org/10.1002/adhm.201601340
73. Atlas Y, Gorin C, Novais A, Marchand MF, Chatzopoulou E, Lesieur J, Bascetin R, Binet-Moussy C, Sadoine J, Lesage M, Opsal-Vital S, Péault B, Monnot C, Poliard A, Girard P, Germain S, Chaussain C, Muller L (2021) Microvascular maturation by mesenchymal stem cells in vitro improves blood perfusion in implanted tissue constructs. Biomaterials 268:120594. https://doi.org/10.1016/j.biomaterials.2020.120594
74. Han J, Luo L, Marcelina O, Kasim V, Wu S (2022) Therapeutic angiogenesis-based strategy for peripheral artery disease. Theranostics 12(11):5015. https://doi.org/10.7150/thno.74785
75. Gao L, Gregorich ZR, Zhu W, Mattapally S, Oduk Y, Lou X, Kannappan R, Borovjagin AV, Walcott GP, Pollard AE, Fast VG, Hu X, Lloyd SG, Ge Y, Zhang J (2018) Large cardiac muscle patches engineered from human induced-pluripotent stem cell–derived cardiac cells improve recovery from myocardial infarction in swine. Circulation 137(16):1712–1730. https://doi.org/10.1161/CIRCULATIONAHA.117.030785
76. Jebran A-F, Seidler T, Tiburcy M, Daskalaki M, Kutschka I, Fujita B, Ensminger S, Bremmer F, Moussavi A, Yang H, Qin X, Mißbach S, Drummer C, Baraki H, Boretius S, Hasenauer C, Nette T, Kowallick J, Ritter CO, Lotz J, Didié M, Mietsch M, Meyer T, Kensah G, Krüger D, Sakib MS, Kaurani L, Fischer A, Dressel R, Rodriguez-Polo I, Stauske M, Diecke S, Maetz-Rensing K, Gruber-Dujardin E, Bleyer M, Petersen B, Roos C, Zhang L, Walter L, Kaulfuß S, Yigit G, Wollnik B, Levent E, Roshani B, Stahl-Henning C, Ströbel P, Legler T, Riggert J, Hellenkamp K, Voigt J-U, Hasenfuß G, Hinkel R, Wu JC, Behr R, Zimmermann W-H (2025) Engineered heart muscle allografts for heart repair in primates and humans. Nature 639(8054):503–511. https://doi.org/10.1038/s41586-024-08463-0
77. Jeon S, Jeong S-H, Lee MH, Seo JW, Kim D-S, Bassous NJ, Lozano Soto JA, Choi C, Gonzalez ML, Nolasco Díaz EB, Kim H, Shin SR, Park J-U (2025) Sustained oxygen-releasing hydrogel implants enhance flap regeneration by promoting mitochondrial biogenesis under mild hypoxia. Bioact Mater 51:559–574. https://doi.org/10.1016/j.bioactmat.2025.04.010
78. Byun H, Han Y, Kim E, Jun I, Lee J, Jeong H, Huh SJ, Joo J, Shin SR, Shin H (2024) Cell-homing and immunomodulatory composite hydrogels for effective wound healing with neovascularization. Bioact Mater 36:185–202. https://doi.org/10.1016/j.bioactmat.2024.02.029
79. Sayed N, Liu C, Wu Joseph C (2016) Translation of human-induced pluripotent stem cells. JACC 67(18):2161–2176. https://doi.org/10.1016/j.jacc.2016.01.083
80. Jeon S, Heo J-H, Myung N, Shin JY, Kim MK, Kang H-W (2024) High-Efficiency, Prevascularization-Free Macroencapsulation System for Subcutaneous Transplantation of Pancreatic Islets for Enhanced Diabetes Treatment. Adv Mater 36(50):2408329. https://doi.org/10.1002/adma.202408329

Authors and Affiliations

Jeonghyun Son[1,2] · Aruzhan Naren[1,3] · Hanan Jamal Mohamed[1] · Minjun Ahn[4] · Won Ha[1,5] · Min Kyeong Kim[1] · Seunggyu Jeon[1,6] · Byoung Soo Kim[4,7,8] · Yoon-Kyoung Cho[1] · Shoji Takeuchi[9,10,11,12] · Hyun-Wook Kang[1]

✉ Hyun-Wook Kang
hkang@unist.ac.kr

[1] Department of Biomedical Engineering, Ulsan National Institute of Science and Technology, Ulsan 44919, Republic of Korea

[2] Department of Bioengineering, Stanford University, Stanford, CA 94305, USA

[3] Max Delbrück Center for Molecular Medicine (MDC), 13125 Berlin, Germany

[4] Medical Research Institute, Pusan National University, Yangsan 50612, Republic of Korea

[5] Department of Plastic and Reconstructive Surgery, Ulsan University Hospital University of Ulsan College of Medicine, Ulsan 44033, Republic of Korea

[6] Department of Bionic Machinery, Research Institute of AI Robotics, Korea Institute of Machinery & Materials (KIMM), Daejeon 34103, Republic of Korea

[7] School of Biomedical Convergence Engineering, Pusan National University, Yangsan 50612, Republic of Korea

[8] Research Institute for Convergence of Biomedical Science and Technology, Pusan National University Yangsan Hospital, Yangsan 50612, Republic of Korea

[9] Department of Mechano-Informatics, Graduate School of Information Science and Technology, University of Tokyo, Tokyo 113-8656, Japan

[10] Department of Mechanical and Biofunctional Systems, Institute of Industrial Science (IIS), The University of Tokyo, Tokyo 153-8505, Japan

[11] International Research Center for Neurointelligence (WPI-IRCN), The University of Tokyo Institutes for Advanced Study, The University of Tokyo, Tokyo 113-0033, Japan

[12] Artificial Cell Membrane Systems Group, Kanagawa Institute of Industrial Science and Technology, Kanagawa 213-0012, Japan